MATERIAL AND MECHANICAL ENGINEERING TECHNOLOGY

Content

Comparative Analysis of Properties of Heat-resistant Alloy Castings Obtained by Different Casting Technologies

Ibatov M.K., Kvon Sv.S., Dostayeva A.M., Medvedeva I.Ye.
Karaganda state technical university, Kazakhstan

Abstract: Some characteristics of castings made of an experimental heat-resistant alloy obtained by the method of casting in sandy-clay molds (SCM) and lost foam casting (LFC) are considered. The microstructures of both castings have been analyzed and their stress-rupture strength has been estimated in the temperature range of 600 ^{0}C – 800 ^{0}C within 50 hours. The tests have shown that despite the same index of contamination, the castings obtained by the LFC method have lower porosity, a more uniform structure, which leads to their higher long-term strength and better mechanical properties.

Keywords: casting, heat-resistant alloy, microstructure, stress-rupture strength, non-metallic inclusions, mechanical properties.

1. Introduction

It is known that the method of producing castings has a decisive influence on the properties of the finished part. Subsequent technological operations, such as, for example, rolling, heat treatment only contribute to the manifestation of the potential capabilities of the product [1].

When casting high-temperature alloys, various methods of casting are used: from SCM (sand-clay molds) to directional crystallization [2, 3]. Selecting the caring technology is determined by the composition of the alloy, the configuration of the casting and technological capabilities of the enterprise. The peculiarity of producing castings of heat-resistant alloys are as follows: a complex chemical composition that causes a wide interval between the liquidus and solidus; features of heat dissipation; a tendency to dendritic segregation. An important requirement to the structure of a heat-resistant alloy is obtaining a homogeneous structure with a sufficiently large grain, since it is the absence of a large number of grain boundaries that prevents the creep development.

For casting the parts of a simple configuration but operating at elevated temperatures under constant loading conditions, low-cost casting methods are used, including those in SCM. Casting in SCM is characterized by a low cost and simplicity of technology, which determines a wide prevalence of the method. However, a low casting yield and a low metallurgical quality of casting in SCM determine the use of other casting methods, even if the cost of production is higher [4].

The essence of the LFC technology consists in gasification of the model under the action of a heat wave emanating from the metal melt. The melt gradually replaces the model and completely repeats its shape. The casting quality is determined by a lot of factors: the quality of the raw materials, the model equipment, the crystallization process. The crystallization process depends on the rate of filling the mold with the melt, which in turn is determined by the burning rate of the material of the model.

2. Results and Discussion

In this paper the studies have been carried out of the casting method effect on the microstructure of the finished casting and, consequently, its properties. The casting (a coupling for valves) has been obtained in two different ways: by casting into single sand-clay molds and by the lost foam method (LFM).

An experimental alloy developed at Karaganda State Technical University has been used as a casting heat-resistant alloy, its chemical composition is given in Table 1.

Table 1 — Chemical composition of the experimental heat-resistant alloy

Name	Elemental composition, %											
	Al	C	Si	Mn	Cr	Ni	Cu	Mo	V	Ti	S	P
Sample	0.062	0.49	0.94	1.01	16.6	0.07	0.09	2.10	1.30	2.2	0.016	0.047

In manufacturing lost foam patterns there has been used construction polystyrene of PSB-25 grade. A factory autoclave has been used for foaming polystyrene.

The finished polystyrene patterns have been covered with a casting (anti-stick) paint of the following composition:
- heat-resistant filler (zircon) – 62 %;
- hydrolytic alcohol - 35.5 %;
- polyvinyl butyral - 2.5 %.

The thickness of the non-stick coating has been 1.8 mm, the drying time 3 hours at the temperature of 600 °C.

The pattern blocks have been suspended vertically in a molding flask measuring 1000×1000×1000. To seal the filler two electric vibrators have been installed that vibrated with the frequency of 36 Hz when filling quartz sand. Then the

casting has been covered with a protective film, and the flask has been evacuated with a side air outlet using a corrugated metal hose.

The casting knockout has been performed after its final solidification, the casting stripping has been carried out in a tumbling drum.

The indicators of the casting quality have been surface cleanliness, geometric accuracy and the value of long-term strength. Table 2 shows the quality indicators of the finished casting obtained according to the developed technology. For comparison, the Table provides the information of the casting quality obtained of the same alloy by the method of casting in sandy-clay molds (the reference sample).

Table 2 – Indicators of the finished casting quality

Sample	σ^{650}_{50}, MPa	Ra, μm	Rz, μm	Overall dimensions	Relative deflection from overall dimensions, %
The reference sample	403	4.80	13.31	Ø176×Ø74×87	3×5×2
The experimental sample	424	5.04	14.62	Ø178×Ø72×84	2×2×2

After complete solidification the castings have been used to produce metallographic sections on which the structure of the alloys has been studied according to the following indicators: the grain size, the non-metallic inclusions index, and segregation. The grain size and the index of non-metallic inclusions have been determined according to GOST 5639-82. The analysis has been carried out in 10 fields of view, in Tables 3, 4 there are the averaged values.

Table 3 – The results of metallographic studies

Sample	Number of grains in circle N_1	Number of grains crossed by circle N_2	Total number of grains in the area of 0.05 mm^2 N_{100}	Average area of the grain A, mm^2	Average diameter D, mm	Grain size acc. to GOST 5639-82
The reference sample	121	37	302	0.0047	0.06	4-5
The experimental sample	125	33	298	0.0051	0.063	4-5

Table 4 – The results of metallographic studies (continuation)

Sample	Amount of the inclusions, %	Average size of the inclusions, μm	Index of inclusions $I_{gen}10^{-3}$	Porosity, %
The reference sample	36	0.027	1.33	5.2
The experimental sample	34	0.039	1.37	4.7

Contamination with non-metallic inclusions is 5 points according to GOST 5639-82 [4]. The same index of contamination is shown by the analysis of the casting structure obtained by the SCM method. Non-metallic inclusions are represented by oxides, nitrides and carbonitrides of chromium, titanium, vanadium, and molybdenum (Figure 1).
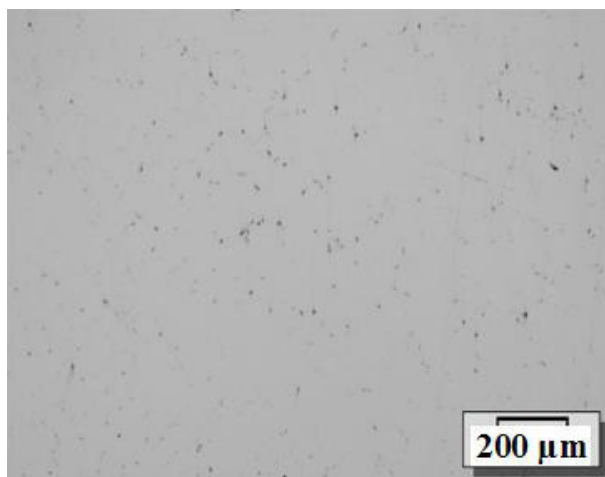
Fig. 1 – Non-metallic inclusions in the casting obtained by the LFC method, ×100

Despite the traditional notions of a lower degree of contamination by non-metallic inclusions in the LFC [5, 6], the contamination index has been almost the same as when casting in sandy-clay molds.

Studying the microstructure for the presence of porosity has shown that with the LFC method` the presence and size of porosity differs from those of casting in sandy-clay molds. The structure when using the LFC is characterized by lower volumetric porosity and a more fine and uniform character of the porosity distribution (Figure 2).

(a)　　　　　　　　　　　　　　　　　　(b)
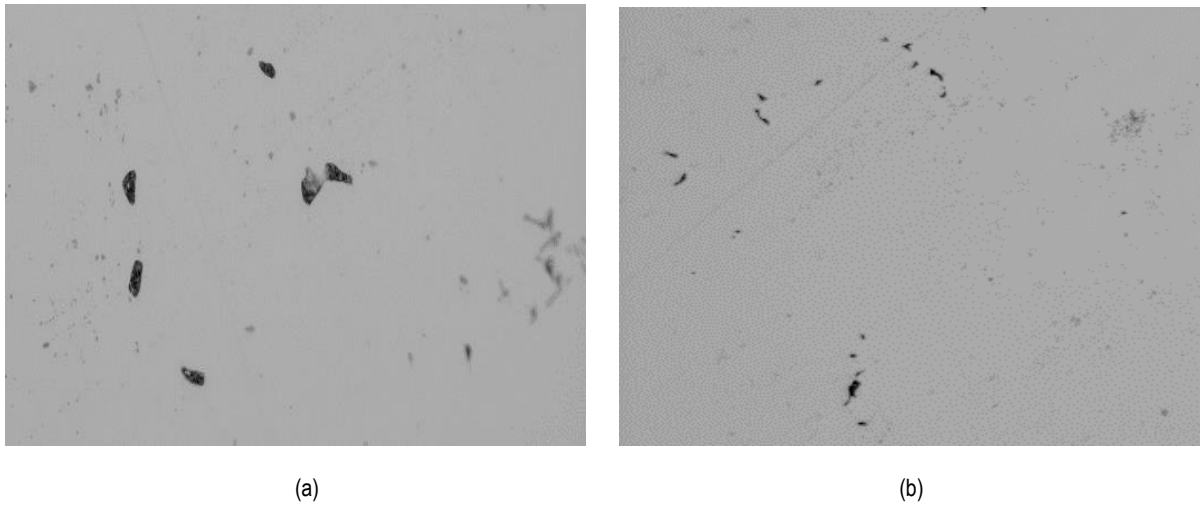
Fig. 2 . Presence of porosity in the structure: a – sandy-clay mold; b – LFC (×500)

The formation of porosity is caused by a lot of factors: the chemical composition, the pouring temperature, the casting method, etc.

It should be noted that porosity of the casting is a hidden defect that is difficult to detect in microscopic studies, even with high magnifications.

In this work porosity of the castings has been studied by mercury porosimetry that allows recording pores with the radius of up to 0.2 nm. The device of the PASCAL 140/440 system has been used in the studies.

The analysis of porograms of castings obtained by different casting methods shows that when casting by the LFC method, the most favorable pore size distribution is manifested: the largest pore volume falls on pores with the radius from 1 to 100 nm, there are practically no pores with the radius of more than 10,000 nm (Figure 3). The presence of fine sieve porosity has a more favorable effect on the strength properties than large porosity with the same pore volume.
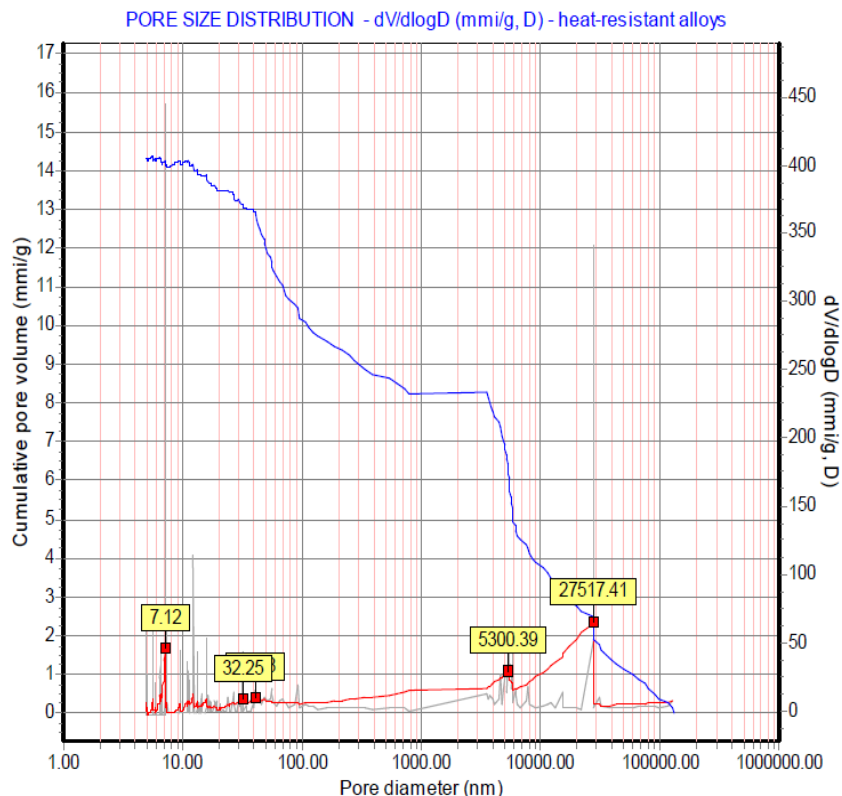
Fig. 3 – Porogram of the casting obtained by the LFC method

The main structure in both castings is presented by the bainite-like matrix with inclusions of complex carbide phases; the matrix hardness is about 53 HRC (Figure 4).

(a)

(b)
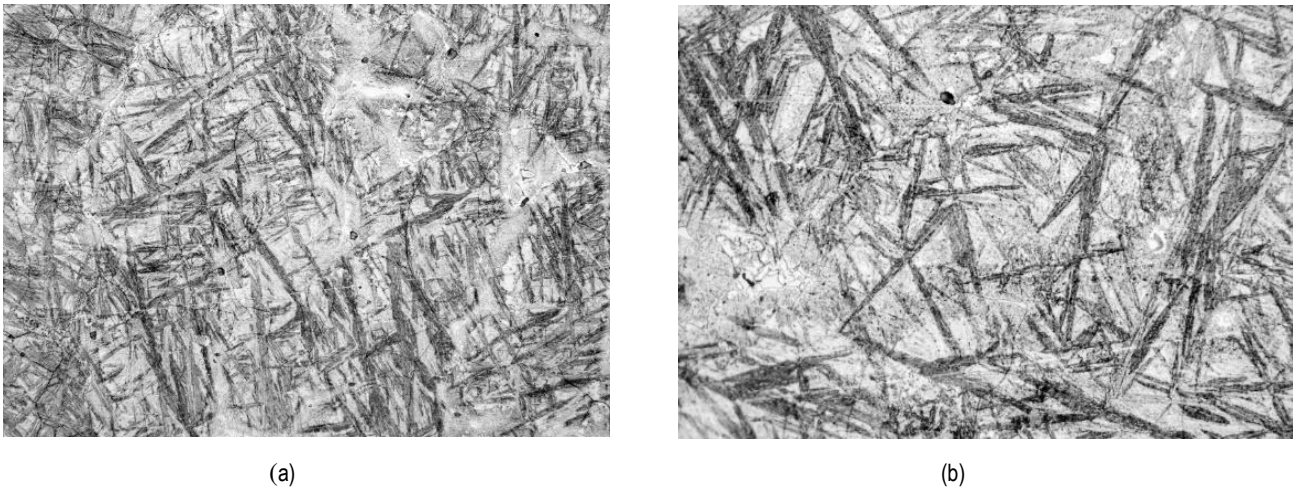
Fig. 4 – Casting microstructure: a – LFC; b – sandy-clay mold (x 1000)

However, the casting microstructure obtained by the LFC method is characterized by higher dispersion of bainite, which should have a positive impact on the mechanical properties.

From castings produced by different casting methods samples have been prepared for stress-rupture strength tests. The tests have been carried out at the temperatures of 600 ^{0}C – 800 ^{0}C within 50 hours.

The tests have been carried out on the test machine TRMP-50-E. The results are presented in Figure 5.
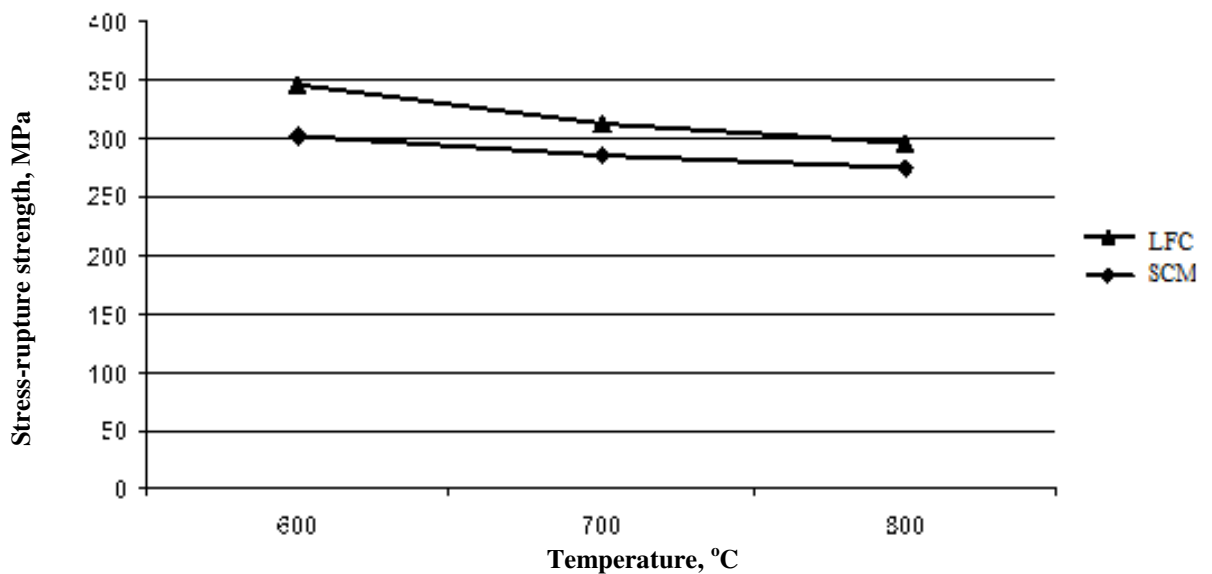
Fig. 5 – Stress-rupture strength dependence on the testing temperature

As it is seen in Figure 5, the results for stress-rupture strength in the specified range for samples obtained by the LFC method are better than for those obtained by the SCM method.

3. Conclusions

In the comprehensive analysis of the data, a definite conclusion can be made: with the LFC the casting structure is characterized by greater homogeneity, lower porosity and higher dispersion of the main matrix. Therefore, despite the same index of contamination in both castings, the level of mechanical properties in the casting obtained by the LFC method must be higher, which has been confirmed experimentally.

Thus, despite the higher cost of the LFC compared to the SCM, the LFC method should be recommended for producing castings of complex-alloyed alloys, since the most significant performance properties, in particular, stress-rupture strength, increase by 13-15 %.

References

[1] Gini E.Ch. Technology of foundry. Special types of casting. M.: Academy, 2008, 380 p.

[2] Superalloys, heat-resistant materials for aerospace and industrial power plants. Edited by C.T. Sims, N.S. Stoloff, W.K. Hagel. M.: Metallurgy, 1995, 456 p.

[3] Issagulov A.Z., Kulikov V.Yu., Kvon Sv.S., Shcherbakova T.V., Kovaleva T.V. Centrifugal casting of heat-resistant alloys. Foundry. 2016. No. 6. P. 20-21.

[4] GOST 1778-70 (ISO 4967-79) Metallographic methods of determining non-metallic inclusions.

[5] Ponomaryova K.V., Deyev V.B., Yudin A.S., Smetanyuk S.V., Nikitina A.A. The influence of density of polystyrene patterns on the quality of castings "gas analyzer housing cover". Proceedings of the XVIII All-Russian Scientific and Practical Conference "Metallurgy: technology, management, innovation, quality", Novokuznetsk, October 14-15, 2014. P. 134-139.

[6] Elinger Z., Weber K. Producing castings of special steels. M.: Nauka, 2006, 226 p.

A Study of the Impact of a Heat-resistant Coating Composition on its Ability to Self-regeneration

Issagulov A.Z., Kulikov V.Yu., Sherbakova E.P., Arinova S.K.
Karaganda State Technical University, Kazakhstan

Abstract: The paper presents the impact of a coating composition on its ability to regenerate. Halloysite clay is proposed to add in the composition of a coating, which, after special treatment, is a source of natural nanotubes. Halloysite nanotubes containing the active substance (heat-resistant coating) enable to slow the release of the active substance, which leads to partial self-recovery of a coating. Laboratory experiments were carried out with simultaneous exposure to temperature, load and oxidizing environment, which confirm the increase in the service life of a coating due to its regeneration. The results of this study also show the impact of the thickness of nonstick paint on the surface quality of a casting made from heat-resistant materials.

Key words: coating, halloysite clay, nanotubes, heat resistance, integrity, regeneration.

1.   Introduction

The main purpose of heat-resistant coatings is to protect products during operation in aggressive environments and increased temperatures. The main reason of failure of any coating is a low adhesive strength, which leads to the delamination of a coating and the violation of its integrity. In a number of works [1, 2] it is noted that quite often secondary reaction zones form on the alloy and heat-resistant coating boundary. This new structural formation is formed by diffusion processes through the "alloy and coating" interface and leads to the softening of a matrix material itself. Therefore, the coating that is applied over a metal product must constitute some obstacle slowing down the diffusion processes. This can be achieved in two ways:
- a coating must be chemically inert with respect to a matrix alloy;
- a coating must be impermeable to diffusion and thus, constitute a barrier to the formation of the secondary reaction zone;

In most studies on the properties of heat-resistant coatings, the focus is on the composition of a coating [3-6]. It is obvious that the composition of a coating is determined, first of all, by the temperature of use; in the second by the composition of a matrix alloy, which is coated. Meanwhile, an analysis of the reasons for the failure of coatings on alloyed steels shows that in most cases the formation processes of secondary reaction zones and, as a result, the failure of a coating occurs at the microdefects localization sites of a coating itself [7]. The presence of microdefects is a catalyst for the development of diffusion processes, which leads to destruction. Meanwhile, it is obvious that the capacity of a coating to recover will reduce the risks of microdefects, reduce the diffusion permeability of a coating, the possibility of secondary reaction zones' formation, which will lead to the preservation of a coating and the surface of a product.

This paper studied the impact of a coating composition on its capacity to regenerate. The study [8] proposes to add in the composition of coating silicon-containing ceramic hollow microspheres, which function as fillers for active constituents. The disadvantage of this composition is a quite large size of silicon-containing hollow microspheres (250-350 microns), which only functions as containers for filling. Compositions based on high-temperature oxides are proposed as contents for filling these containers. During operation, contents of a container release at once, as a result, a coating is formed. Further regeneration of a coating is impossible, since containers emptied. In other words, there is no material to restore the integrity of a coating.

 A number of papers [9-11] note that the natural material, halloysite clay, is a material containing natural nanotubes. Unlike many other nanotubes, halloysite tubes are almost a natural product, available in thousands of tons, including our Republic. Halloysite nanotubes are proposed as a nanocontainer for loading, storing, and controlled release of heat-resistant composition.

Natural halloysite clay is mined in the form of pieces of various sizes and different humidity. Before using clay as a component of the composition, it must undergo the necessary preparation, which consists in drying at a temperature of 40 - 50 ° C to obtain the required moisture (no more than 5%) and further mechanical grinding. Fractional composition after grinding is fraction -2 microns not less than 80%. Such a fractional composition ensures the largest "opening" of natural halloysite nanotubes, which are containers of active substances.

The prepared coating with a thickness of approximately 0.3 - 0.5 mm is applied using a special unit on a metal product. After application, the surface is dried at room temperature until completely dry. The use of a heat-resistant coating using halloysite clays increases the service life of a coating by 20 - 30% depending on the conditions of working environment.

2. Results and Discussion

According to the above method, researches were carried out at the Center of heat-resistant materials laboratory of Karaganda State Technical University to study the properties of a heat-resistant coating using halloysite nanotubes. As a standard, the composition was used that included heat-resistant metal oxides (TiO2) in an amount of 30%, silica in a finely crumbled up form (20%) in a solution of an alkali metal silicate and silicon-containing ceramic hollow microspheres (32%).

The composition of the makeup was applied over a development type, i.e., heat-resistant metal oxides (TiO_2) in an amount of 30%, silica in a finely crumbled up form (20%) in a solution of an alkali metal silicate and prepared halloysite clay in an amount of 30%. Mixing was carried out under vacuum of 0.4 kPa for 15 minutes, the temperature of mixing was 24 °. To obtain the mixture, a non-standard installation was used, including a vacuum mixer, into which the mixture components were fed. The mixer has a thin mill that allows you to mix and simultaneously grind coarse particles of the mixture.

The test compositions were applied to the standard and the development type using a hand-held spray gun. To estimate the mechanical properties, a set was used to determine the mechanical properties using a furnace, the heating in which was carried out using electric heaters. Then the standard and the development type were destroyed under a load of 400 MPa at a temperature of 600 °C in an atmosphere of air (oxidizing environment), and at the same time the integrity of a coating was controlled. The integrity of a coating was determined using PG – 33430 Byko-cutuniversal with increasing X20. The integrity of a coating on the standard was destroyed after 4 hours, on the development type after 5.2 hours. The increase in the integrity life of a coating is due to the slow release of active heat-resistant components made from halloysite nanoconeiners, which leads to self-regeneration of a coating during a certain time. Figure 1 show data on the impact of test temperature and pressure on the integrity of a coating.

Figure 2 show the impact of pressure applied to the sample during the operation of a coating.
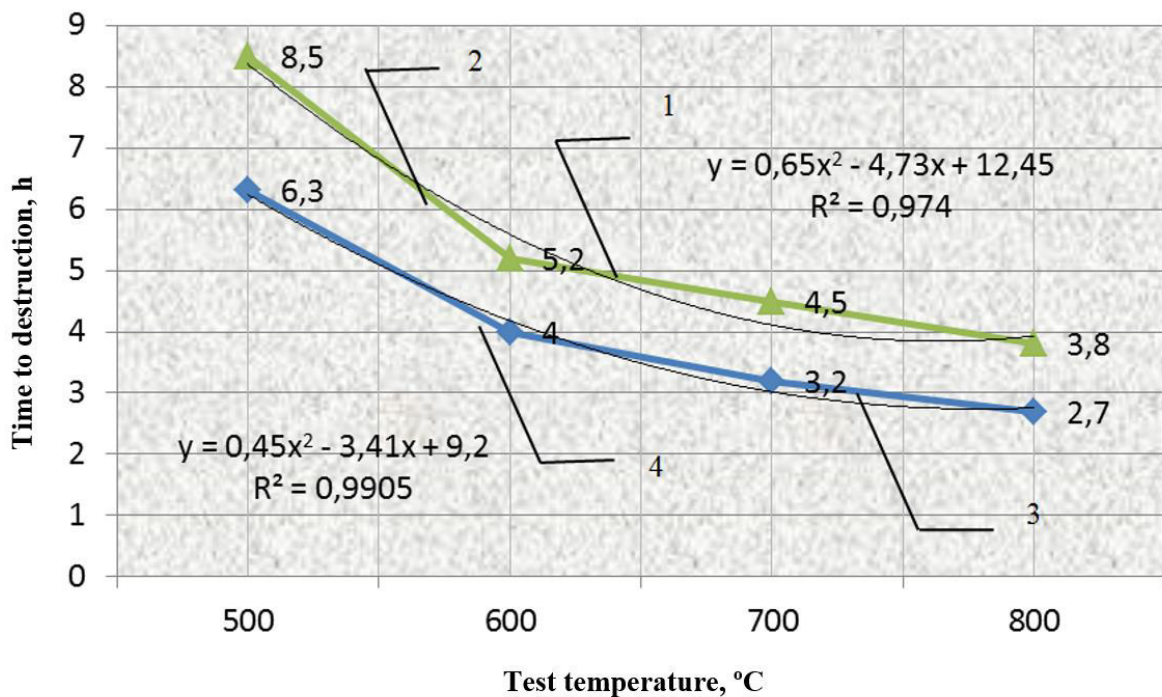
Fig. 1 - Dependence of time to coating's destruction from test temperature: 1 - time to destruction of an experimental coating, h; 2 - the calculated line of a curve 1; 3 - time to destruction of the standard alloy, h; 4 - the calculated line of a curve 3

The graph shows the experimental regression line (curve 1). The calculated regression line (curve 2) was set up using the equation $y = 0.65x^2 - 4.73x + 12.45$ with a validity coefficient $R^2 = 0.974$. The graph also shows the experimental regression line (curve 3). The calculated regression line (curve 4) is set up according to the equation $y = 0.45x^2 - 3.41x + 9.2$ with a validity coefficient $R^2 = 0.9905$.

The graph shows the experimental regression line (curve 1). The calculated regression line (curve 2) is set up according to the equation $y = 1.375x^2 - 10.665x + 24.925$ with a validity coefficient $R^2 = 0.9997$. The graph also shows the experimental regression line (curve 3). The calculated regression line (curve 4) is set up according to the equation $y = 0.6x^2 - 5.56x + 15.4$ with a validity coefficient $R^2 = 0.9991$.

$$y = 1{,}375x^2 - 10{,}665x + 24{,}925$$
$$R^2 = 0{,}9997$$

$$y = 0{,}6x^2 - 5{,}56x + 15{,}4$$
$$R^2 = 0{,}9991$$
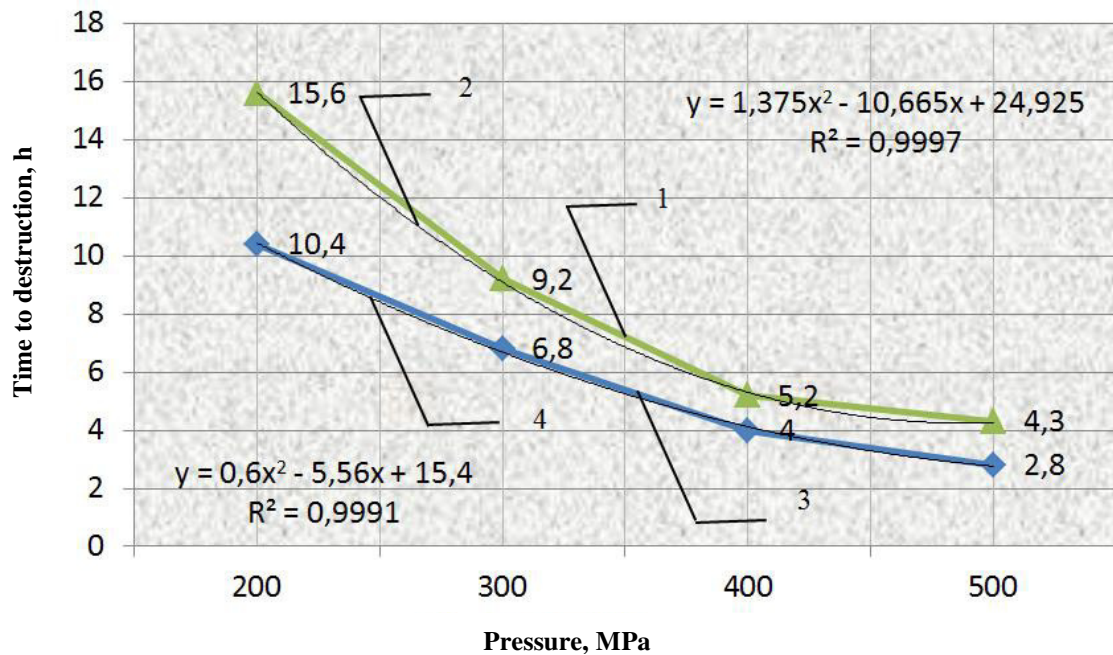
Fig. 2 - Dependence of time to destruction of a coating from pressure on a sample: 1 - time to destruction of an experimental coating, h; 2 – the calculated line of a curve 1; 3 - time to destruction of the standard alloy, h; 4 - the calculated line of a curve 3

The impact of the thickness of nonstick paint on the surface quality of a casting from heat-resistant materials was also studied. The thickness of a nonstick coating (paint) has a direct impact on the surface quality, which is first of all due to gas permeability of a coating, which in turn determines the burning rate of a model [12, 13]. To determine the optimal thickness of applying a nonstick coating, studies have been carried out on the interrelation between the coating thickness (paint), the drying time of a coating, gas permeability of a coating and surface roughness of a casting. Nonstick coating was applied to a polystyrene model using a coating machine (spray gun) and a brush. Coating thickness ranged from 0.75 to 2 mm. Models' drying with paint was carried out in a special dryer in a stream of hot air, the drying time was changed from 0.5 to 5 hours. The composition of the used nonstick paint is shown on table 3.

The roughness was measured with a portable TR 100 roughness tester according to GOST 2789 - 73 [14].

Gas permeability of a model with a paint skin was determined on the device for determining gas permeability of a model 04315M (AUSS 29234.11-91).

The data obtained are shown on graphs (Figure 3-8).

Table 3 – The composition of nonstick paint for castings from a heat-resistant alloy, mass: %

Fireproof filler Zircon	Hydrolyzed alcohol	Polyvinyl butyral	Density, g / cm³	Casting type
62	35.5	2.5	1.7-1.84	Casting on gasified models, an experimental heat-resistant alloy

Castings roughness was determined with a coating thickness of 2 mm in a casting model, depending on time and temperature of drying (Figure 3). It was determined that the thickness of a nonstick paint skin on the polystyrene model should be directly proportional to the sand-shaped porosity, temperature of a casting metal and its hydrostatic pressure during casting. At the same time, it is important that gas permeability of paints has to be technologically necessary. A paint skin with a thickness of 1.2-2.0 mm is recommended for castings made from heat-resistant alloys. The greater the metalostatic pressure during casting and the temperature of a metal, the greater should be the thickness of paint while maintaining its gas permeability [15].

Figure 3 shows the calculated and experimental the dependence curves of surface roughness on the thickness of the applied paint. The graph shows the experimental regression line (curve 1). The calculated regression line (curve 2) is set up according to the equation $y = 3.5893x^2 – 36.239x + 143.9$ with a validity coefficient $R^2 = 0.9841$.

11
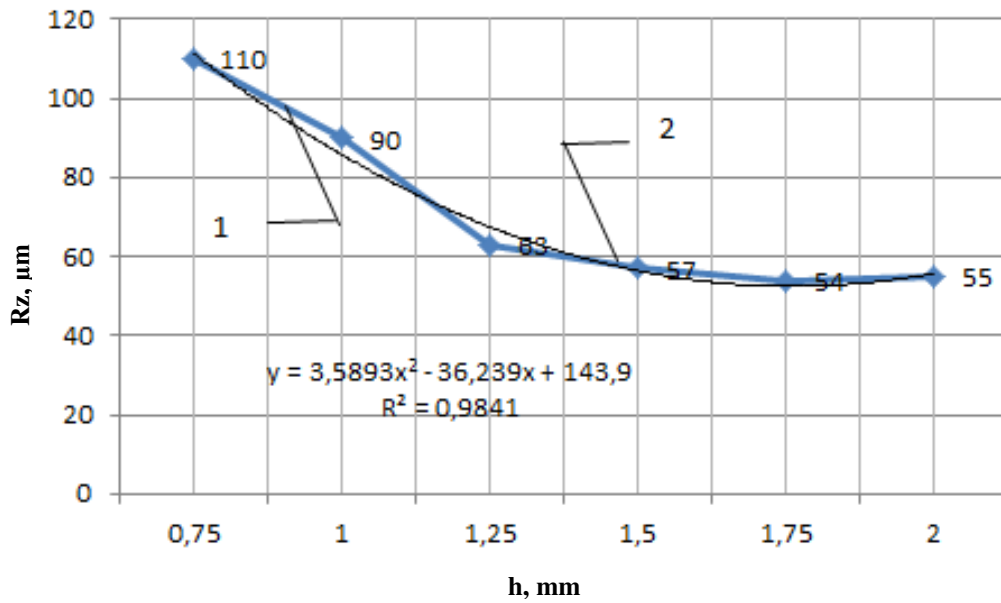
Fig. 3 - Dependence of casting roughness on the thickness of a non-stick paint skin

The graph shows that an increase in the thickness of the paint skin from 1.6 to 2 mm has no impact on surface roughness and remains almost unchanged (about 55 microns), which is satisfactory for the surface of a casting.

Figure 4 shows dependence of gas permeability of a model with paint, depending on the thickness of the applied paint.

The graph shows the experimental regression line (curve 1). The calculated regression line (curve 2) is set up according to the equation $y = 0.2321x^2 - 7.625x + 134.5$ with a validity coefficient $R^2 = 0.9142$.

As expected, the value of gas permeability is inversely proportional to the thickness of a coating. However, starting with a value of 1.6 mm, the thickness of a coating virtually has no impact on the gas permeability, this value ranges from 98-100 units.
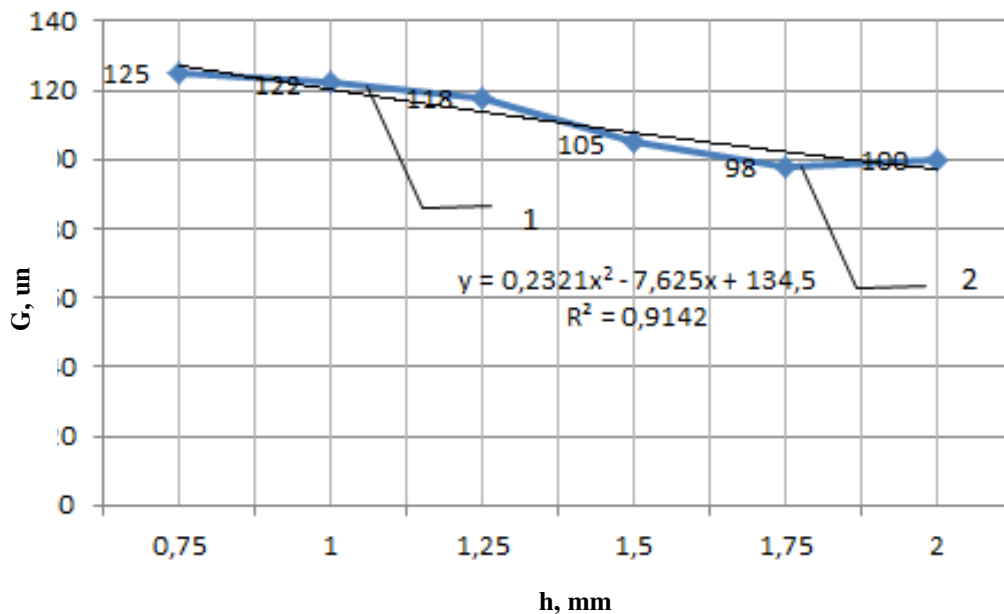
Fig.4 - Dependence of gas permeability of a model on the thickness of a paint skin on it

It is obvious that the roughness of a finished casting depends on the roughness of a model. Studies have confirmed this position. As can be seen from Figure 5, dependence of surface roughness of a casting on surface roughness of a model is linear and is expressed by the dependence:

R_Z casting = R_Z pattern + (30 ... 40 microns).
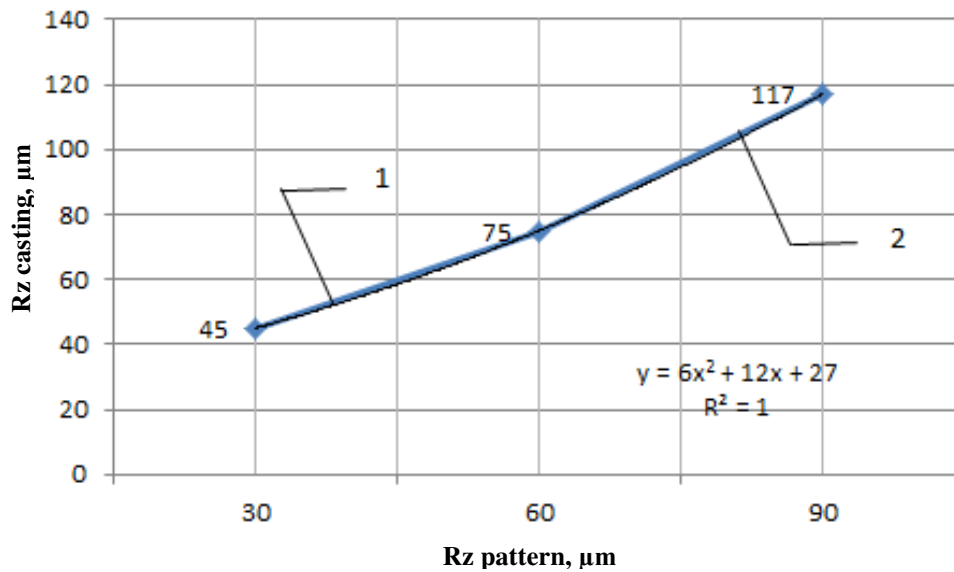
Fig. 5 - Dependence of the roughness of castings on the roughness of models

The graph shows the experimental regression line (curve 1). The calculated regression line (curve 2) is set up according to the equation $y = 6x^2 + 12x + 27$ with a validity coefficient $R^2 = 1$.

The results of experimental data to determine dependence of the burning-on value of a casting on the thickness of a paint skin on a polystyrene model are shown in the graph (Figure 6). In the range from 1.5 to 2 mm, the burning-on value is minimal and amounts to 0.12 g / cm^2. Then, with an increase in the thickness of a coating, the burning-on value increases by about 9.5%.

The graph shows the experimental regression line (curve 1). The estimated regression line (curve 2) is constructed according to the equation $y = 0.0479x^2 - 0.4093x + 0.92$ with a confidence coefficient $R^2 = 0.7953$.

The impact of the paint drying time on surface roughness values is shown interestingly (figure 6). The studied time interval was 0.5-5 hours. The drying temperature was kept constant at 600 °C. As can be seen from the graph, with increasing drying time to 3-3.5 hours, surface roughness decreases, then after 3.5 hours surface roughness begins to grow. This fact can be explained by the burnout of paint components and related surface destruction, which negatively impacts the cleanliness of casting surface.
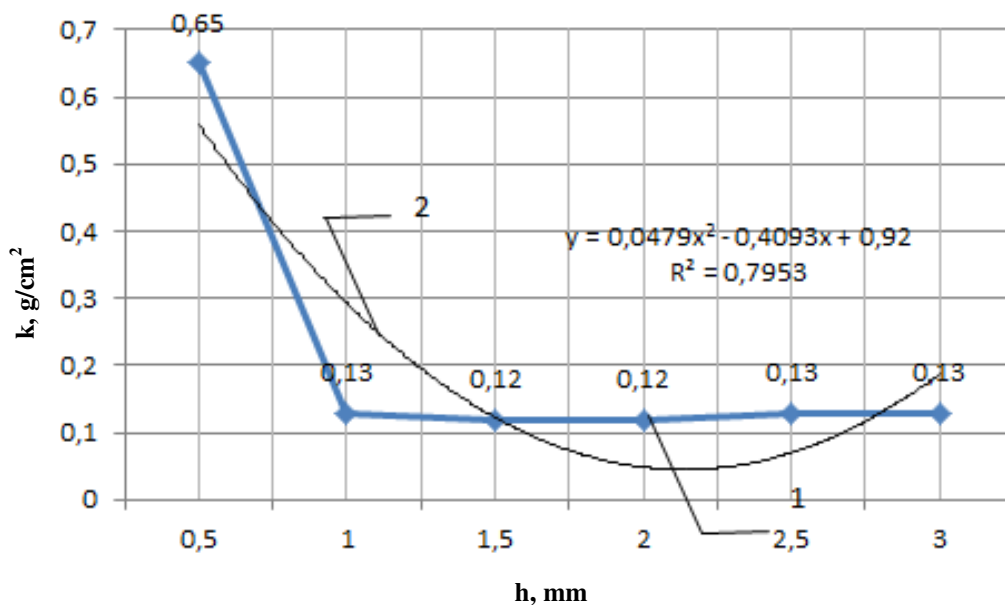
Fig.6 - Dependence of the burning-on value of a casting on the thickness of a paint skin on a polystyrene model

The drying temperature also has a direct impact on the surface quality of a casting. The drying temperature was varied from 30 to 800 ° C. The drying time was maintained constant, 2.5 hours. The unexpected fact was that an

increase in the drying temperature, even with a decrease in the isothermal holding time, increases the roughness of castings. Apparently, an increase in temperature as well as an increase in the holding time of more than 3.5 hours leads to the decomposition of paint components and surface destruction.

Figure 7 shows the calculated and experimental curves of dependence of surface roughness on the time of drying. The graph shows the experimental regression line (curve 1). The calculated regression line (curve 2) was set up according to the equation $y = 2.625x^2 - 22.604x + 121.3$ with a validity coefficient $R^2 = 0.9664$.
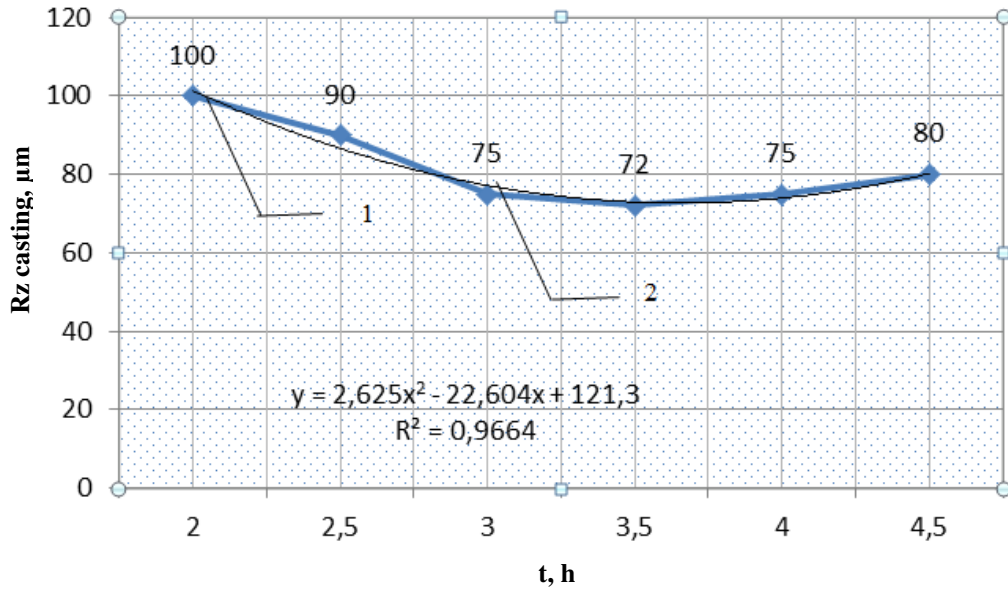
Fig. 7 - Dependence of the roughness of the casting on the time of drying paint

Figure 8 shows the calculated and experimental curves of dependence of surface roughness on the temperature of paint drying. The graph shows the experimental regression line (curve 1). The calculated regression line (curve 2) is set up according to the equation $y = 4.0714x^2 - 33.9x + 138.4$ with a validity coefficient $R^2 = 0.9184$.
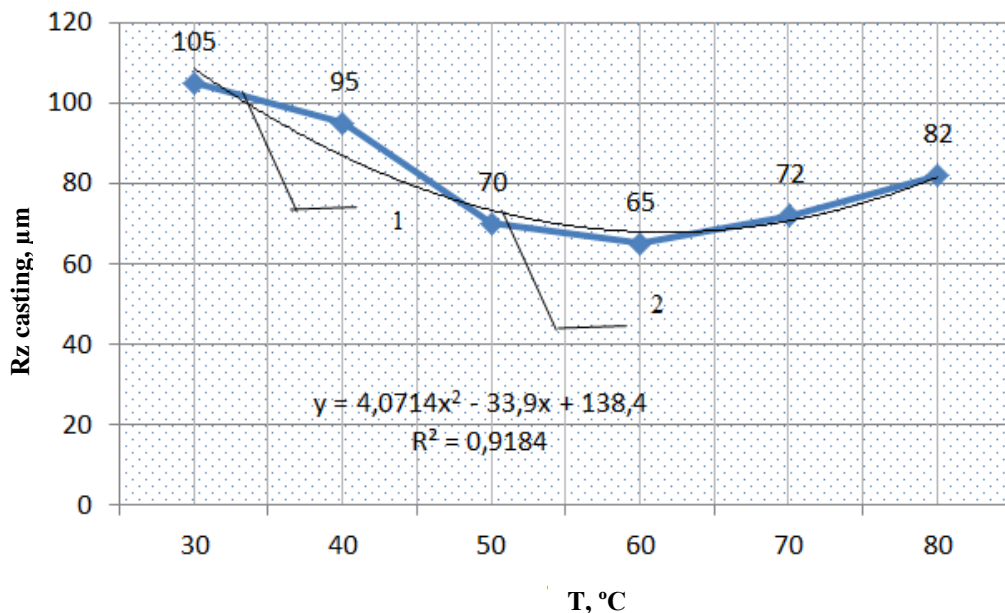
Fig. 8 - Dependence of casting roughness on the temperature of paint drying on a polystyrene model

3.   Conclusions

The studies show that the addition of natural halloysite nanotubes into the composition of a heat-resistant coating enables to increase its service life due to self-regeneration processes. There is proposed the composition of a coating

containing heat-resistant metal oxides (TiO_2) in an amount of 10-30%, silica or heat-resistant aluminosilicate in a finely crumbled up form (8-20%) in a solution of an alkali metal silicate, and additionally containing halloysite clay in a percentage ratio of 20-30% by weight.

Studies have shown that the optimal parameters in the manufacture of castings from heat-resistant alloys using the method of casting on gasified models are the following:

- non-stick coating thickness: 1.6 - 2mm;
- drying time: 3 - 3.5 hours;
- drying temperature: 600 °C.

References

[1] Gayamov A.M., Budinovskiy S.A., Muboyadzhyan S.A., Kosmin A.A. Vybor zharostoykogo pokrytiya dlya zharoprochnogo splava marki VZHM 4 //Trudy VIAM, № 1, 2014. - p. 13-18

[2] Muboyadzhyan S.A., Budinovskiy S.A., Gayamov A.M., Matveyev P.V. Vysokotemperaturnyye zharostoykiye pokrytiya i zharostoykiye stali dlya teplozashchitnykh pokrytiy. Aviatsionnye materialy i tekhnologii, № 1, 2013. - p. 17 - 23

[3] Patent RF 2320689. Sostav zharoprochnogo pokrytiya.

[4] Selent Marcel, Abendroth Martin, Kuna Meinhard //Transactions of the Indian institute of metals, № 2, vol. 69, 2016. - p. 629-633.

[5] Thorat P.V. //Int. J. of Eng. Sc. & Adv. Tech., Vol. 3, Issue-5, 2013. – p. 243-250

[6] Patent US6436543 B1. Sostav zharoprochnogo pokrytiya.

[7] Kashin D.S., Stekhov P.A. Razrabotka kompleksnykh zharostoykikh pokrytiy dlya detaley iz yestestvenno-kompozitsionnogo materiala na osnove niobiya. //Trudy VIAM, № 6, 2017. – p.3-12

[8] Patent RU 2311397. Sostav zharoprochnogo pokrytiya.

[9] Kristallograficheskaya baza dannykh mineralov MINCRYST

[10] http://naturalnano.com/products-technologies/halloysite-nanotubes/

[11] Jin-Woo Lee,Soo-Jeong Park ,Yun-Hae Kim. Improvement of Interfacial Adhesion of Incorporated Halloysite-Nanotubes in Fiber-Reinforced Epoxy-Based Composites. // Applied Sciences, 7(5), 441, 2017. – p.1-8

[12] Illarionov I.E., Strelnikov I.A., Bakirov R.B., Shalunov Ye.P., Korolev A.V., Moiseyeva O.V. Sovremennoye sostoyaniye polucheniya sterzhney, form i protivoprigarnykh pokrytiy dlya otlivok iz chernykh i tsvetnykh metallov i splavov // Materialy II-oy mezhdunarodnoy nauchno-prakticheskoy konferentsii «Sovremennyye tekhnologii v mashinostroyenii i liteynom proizvodstve», Cheboksary, 2016. - p. 36-47.

[13] Kukuy D.M., Nikolaychik Yu.A., Filimonenko R.S. Zakonomernosti formirovaniya strukturno-mekhanicheskikh svoystv protivoprigarnykh pokrytiy, modifitsirovannykh nanostrukturirovannymi materialami // Lit'ye i metallurgiya, № 1 (69), 2013. - p. 43-47.

[14] GOST 2789-73 Sherokhovatost poverkhnosti. Parametry i kharakteristiki.

[15] Gayamov A.M., Budinovsky S.A. Study of the influence of the thickness of the barrier layer of the coating on the properties of the compositions of heat resistant alloys VZHM1 and ZhS36 with a heat-resistant coating // Trudy VIAM, № 9, 2014. - p. 3-10

The Selection of Envelope Amplitude of the Sweep signal force

Moyzes B.B.[1], Gavrilin A.N.[1], Zhetessova G.S.[2]
[1]National Research Tomsk Polytechnic University, Russia
[2] Karaganda State Technical University, Kazakhstan Republic

Abstract. Vibrational seismic exploration is based on the vibrational seismic sources which excite and transmit specific sweep signals to the ground. Informative signal parameters depend on the sweep signal parameters, one of which is the law of signal amplitude variation. The purpose of this research is to determine the influence of sweep signal amplitude variation law on the rate of valuable information release on correlation with background noise. The work also assesses the influence of the law of the sweep signal envelope formation on the sweep signal autocorrelation function that affects significantly the efficiency of the vibroseis works.

Keywords: vibroseis works, sweep signal, envelope amplitude, autocorrelation function, accuracy of the envelope formation

1. Introduction

Pulse, pulse-code and vibrating mechanisms are used in seismic exploration [1–3]. Each type of source has advantages and disadvantages. Vibration sources have a larger perspective provided the reduction of overall weight, which limits their application. Vibration sources excite and transmit mechanical forces with certain properties – sweep signals to the ground.

During seismic exploration, the signals with the best parameters are searched, such as follows: sufficient energy, broadband frequency spectrum providing a compact autocorrelation function (ACF), the steadiness of these properties after repeated radiation in different locations [4].

2. Envelope amplitude of the sweep signal

In modern vibrational seismic exploration, the best parameters have linear frequency-modulated signals, which are described by the following relationship [5, 6]:

$$x(t) = A(t)\sin\left(\frac{\varepsilon t^2}{2} + \omega_0 t + \varphi_0\right), \tag{1}$$

where $A(t)$ – the signal oscillation amplitude,
t – current time;
ω_0 – initial frequency of sweep signal;
φ_0 – initial phase,
ε – frequency buildup rate, which is:

$$\varepsilon = \frac{\omega_{ef} - \omega_0}{T_0}, \tag{2}$$

where ω_{ef}, ω_0 – end and initial frequency of sweep-signal;
T_0 – sweep-signal time, which is as follows:

$$T_0 = t_{et} - t_0, \tag{3}$$

where t_{et}, t_0 – end and initial sweep-signal time.

At each moment of frequency ramp (e = const.) (Figure 1) there is a correspondent frequency, which is found in the frequency range only once. The signal transmitted to the ground at time $0 \dots t$ is informative only during the sweep-signal excitation T_0.
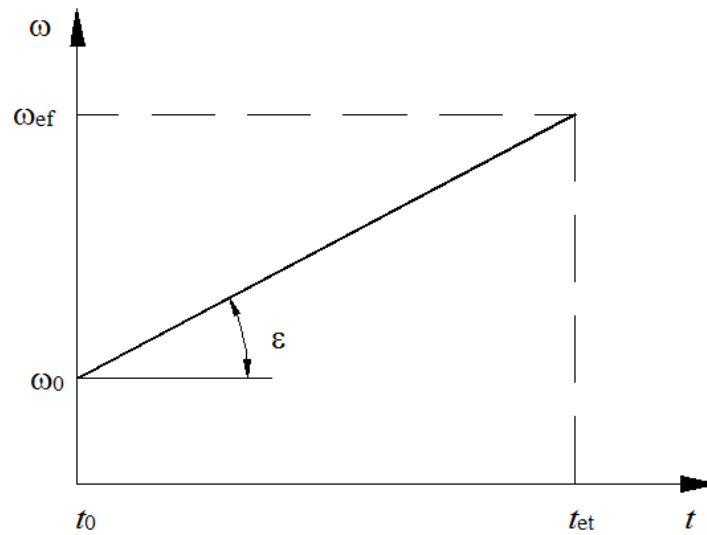
Fig. 1. - The law of signal frequency change

During the time period $0...t_0$ signal frequency – ω is equal to ω_0. During the time period $t_{et}...t$ the signal frequency – ω is equal to ω_{ef} (Figure 2).
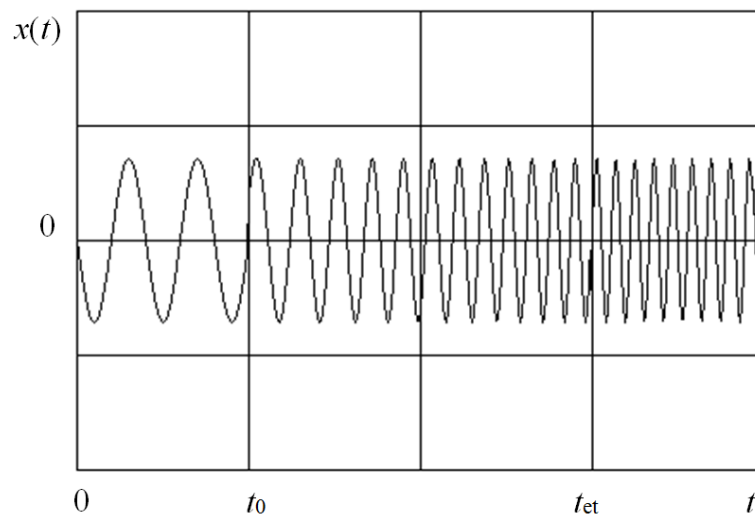
Fig. 2. - Signal waveform

Sweep-signal is transmitted to the ground and then summed with the waves which produced by quasi-harmonic power in the medium. This results a formation of a complex vibration pattern also influenced by reflection from the internal boundaries. It is almost impossible to determine visually the time of arrival of the reflected sweep-signal.

The correlation and frequency methods of signal processing are used to distinguish the valuable information. The correlation method is easier to implement. This method is implemented by calculating the correlation integral (4), namely, by finding the cross-correlation function (CCF):

$$r(\tau) = \frac{1}{T_0} \int_{t_0}^{t_{et}} x_1(t) x_0(t - \tau) dt, \tag{4}$$

where x_1, x_0, T_0, τ – accordingly adopted (reflected) and the original signals, the signal period and the time shift at the signals correlation.

Assuming that the reflected signal received by the receiver is not distorted, its cross-correlation function is ideal (in this case, the autocorrelation function ACF) (Figure3) with a well-defined main peak 1 on the background of the side 2.
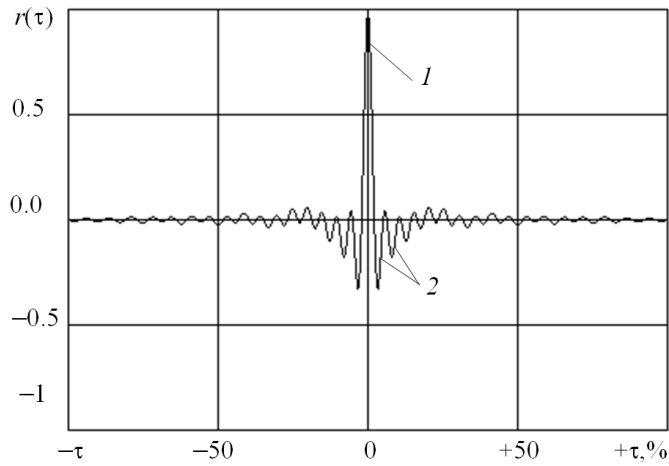
Fig. 3. - Ideal cross-correlation function

To increase the accuracy of estimated and registered signal relatively to the original signal:

$$x(t) = [A(t) + \Delta A(t)] \sin \left(\frac{\varepsilon + \Delta \varepsilon}{2} t^2 + (\omega_0 + \Delta \omega_0)t + (\varphi_0 + \Delta \varphi_0) \right) \quad (5)$$

and CCF:

$$r(t) = \frac{1}{T_0} \int_{t_0}^{t_{et}} x_0(t)x_0(t - \tau)dt, \quad (6)$$

it is necessary to meet the following requirements:

• should tend to zero: the oscillation amplitude error ΔA, the rate of the frequency rise error $\Delta \varepsilon$, the initial frequency $\Delta \omega_0$ and phase $\Delta \varphi_0$ (5) error;

• should have a well-defined, quickly extinguishing main peak, ACF sweep (Figure 4);

• should not cross the conventional line 3 ACF peak.

Because ACF is symmetrical in relation to its argument τ it is accepted to consider only half of the graph (Figure 4) while studying ACF.
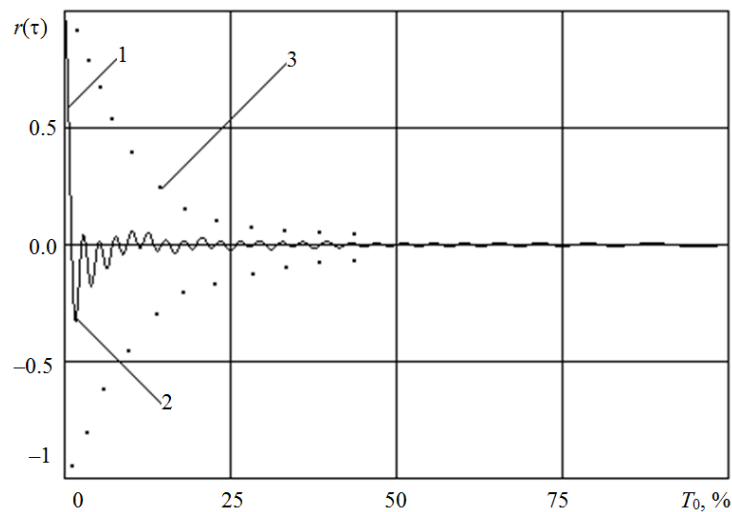
Fig. 4. - Autocorrelation function

Some research articles describe the possibilities to form the linear frequency-modulated signals both with a constant and time-variable oscillation amplitude of the impact force A, so-called amplitude-modulation signals (AM-signals).

18

It is noted in the sources of information [6] that the amplitude and frequency of side peaks directly depend on the law of envelope variation of the AM signal. The signals with rectangular envelope (Figure 2), are widely used in modern seismic exploration works, due to the relative simplicity of the method. These signals have the greatest intensity of side peaks.

Therefore, the aim of this research is to work out the low of amplitude modulation of the sweep signal and its parameters, causing the most compact ACF.

3.   The selection of amplitude envelope of sweep-signal force

Time-bandwidth product is one of the main parameters of sweep-signal and it affects the quality of signal processing:

$$TBWP=\Delta\omega T_0, \tag{7}$$

where $\Delta\omega$ – frequency deviation.

Following parameters are set up for the research: $\Delta\omega$=140 Hz T_0=0.1 s (rationale for choosing is given below) TBWP=14 (7).

On the base of specific law of the envelope change (Figures 5-10) it can be concluded that the signal with the envelope shape close to a sinusoidal (Figures 9, 10) comes with the best parameters. It is possible to achieve more compact ACF by increasing by frequency of the time-bandwidth product if frequency deviation is changed. For example, twice – TBWP=28 (Figure 10).
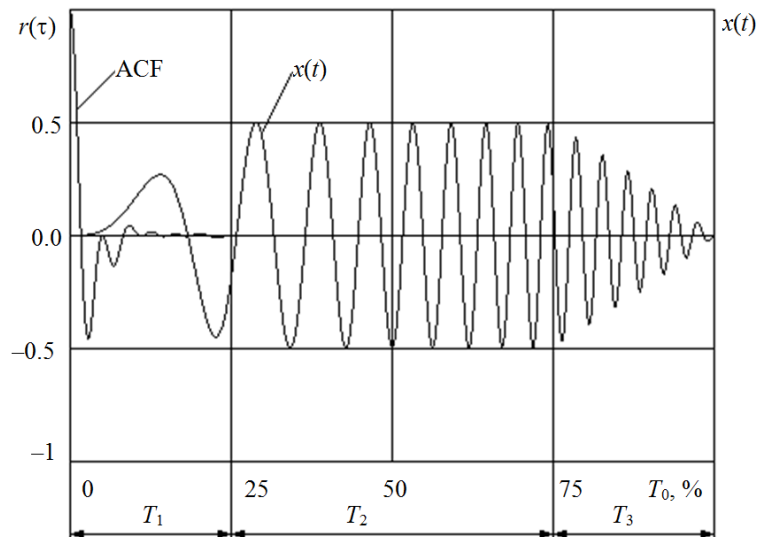
Fig. 5. - Sweep signal with the trapezoid form of envelope (TBWP=14)
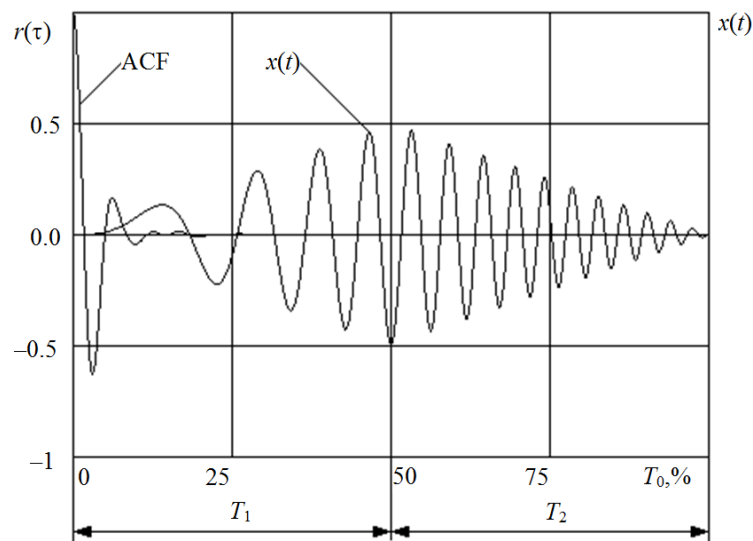
Fig. 6. - Sweep signal with the rhombic form of envelope (TBWP=14)

19
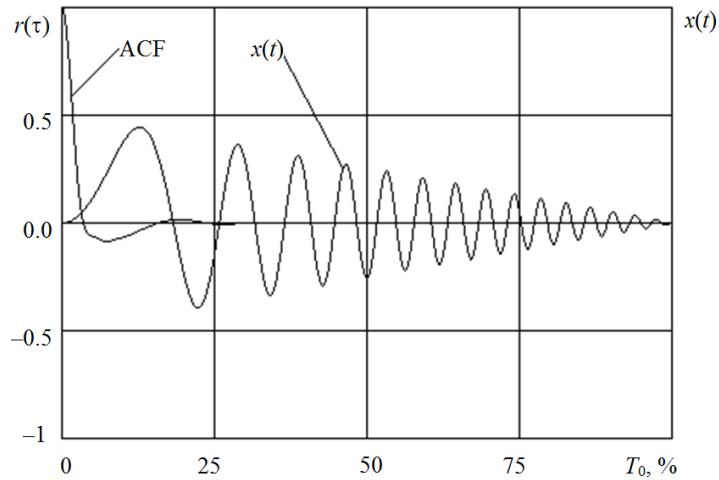
Fig. 7. - Sweep signal with the triangle $T_2=T_0$ (TBWP=14) form of envelope
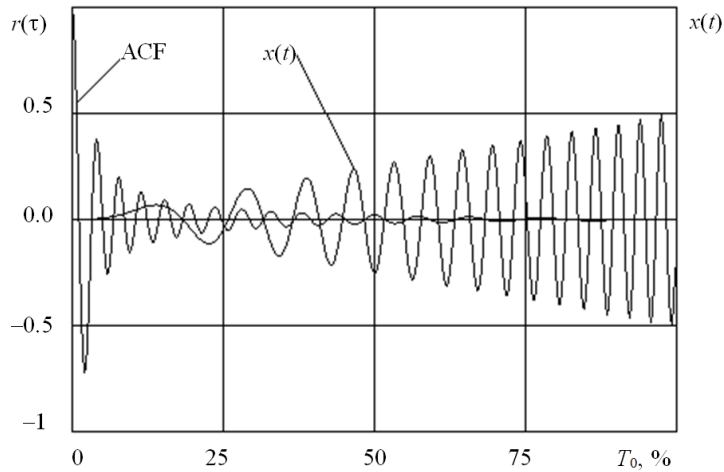
Fig. 8. - Sweep signal with the trigonal $T_1=T_0$ (TBWP=14) form of envelope

When the level of side peaks reduced the noise immunity of the method deteriorates due to drop of total energy transferred to the ground. In this case, the methods of source grouping and the effects accumulation are used which helps to receive more useful information. In practice, the signals used within the range of 10…250 Hz , with value of the time-bandwidth product of TBWP = 100…300 and duration of 20…30 seconds.

Therefore, in our case it is necessary to emit a signal at least n times (use the accumulation of impacts):

$$n = \frac{100^2}{14^2} \approx 51.$$

Fig. 9. - Sweep signal with the sinusoidal form of envelope (TBWP=14)

Fig. 10. - Sweep signal with the sinusoidal form of envelope (TBWP=28)

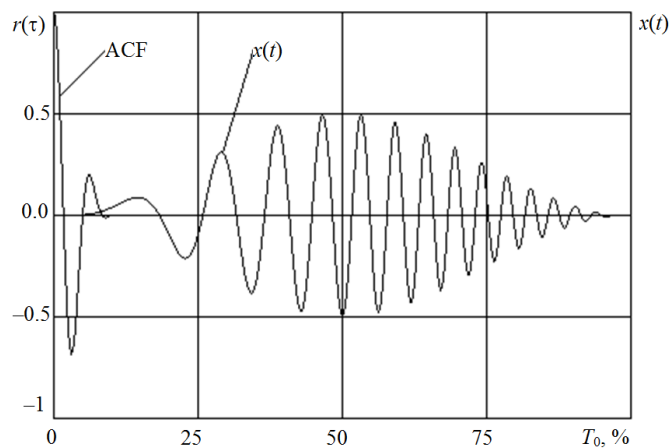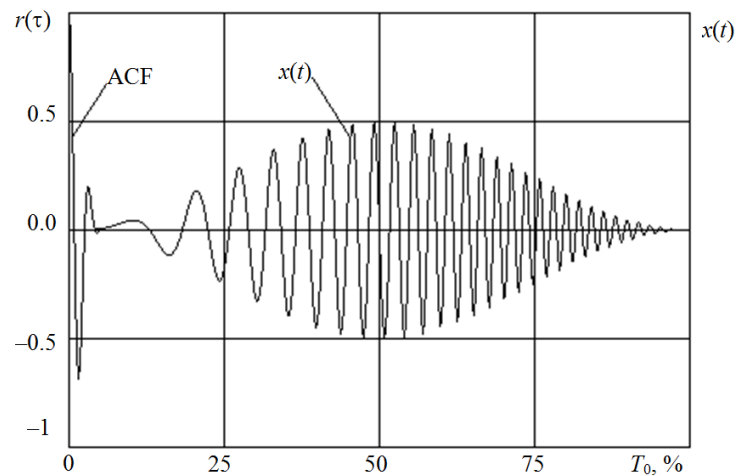## 4.   Conclusion

The influence of law of change of the amplitude envelope of sweep-signal force on the compactness ratio of the ACF was analyzed during the performed simulation. It is concluded that the implementation of signals with the sinusoidal law of envelope change (compared with other signals) is more viable due to the most compact of ACF and the best rate of valuable information release.

Based on the above we can conclude that it is rather viable to produce the vibration source of seismic oscillations with a compact ACF and smooth envelope of effort amplitude and which has a relatively low weight.

To creating a light weight vibrating source it is necessary to combine the active system of the support area clamping to the ground [4] and the vibration actuator [1].

Therefore, further research will be focused on the development and study of the vibrosource design options. The source must generate the sweep signal with a sinusoidal waveform amplitude envelope.

Reference

[1] Moyzes B.B. et al. Actuators of the Seismic Vibrations Sources // Mechanical Engineering, Automation and Control Systems: proceedings of the International Conference, Tomsk, 1-4 December, 2015; Institute of Electrical and Electronics Engineers. – Article number 7414967. DOI: 10.1109/MEACS.2015.7414967.

[2] Poletto F., Schleifer A., Zgauc F., Meneghini F., Petronio L. Acquisition and deconvolution of seismic signals by different methods to perform direct ground-force measurements // Journal of Applied Geophysics, Vol. 135, 2016. – p. 191-203.

[3] Richter H., et al. Comparison of pneumatic impact and magnetostrictive vibrator sources for near surface seismic imaging in geotechnical environments // Journal of Applied Geophysics, Vol. 159, 2018. – p. 173-185.

[4] Moyzes B.B. et al. The System of Clamping the Base Plate of the Seismic Vibrations Sources to the Ground // Mechanical Engineering, Automation and Control Systems: proceedings of the International Conference, Tomsk, 1-4 December, 2015; Institute of Electrical and Electronics Engineers. – Article number 7414968. DOI: 10.1109/MEACS.2015.7414968.

[5] Gavrilin A.N. et al. Land-based sources of seismic signals // Mechanical Engineering, Automation and Control Systems: proceedings of the International Conference, Tomsk, 16-18 October, 2014; Institute of Electrical and Electronics Engineers. – Article number 6986947. DOI: 10.1109/MEACS.2014.6986947.

[6] Shneerson M.B., Potapov O.A., Grodzenskij V.A. Vibratsionnaya sejsmorazvedka [Vibroseis works]. - Moscow: Nedra, 1990. – 240 p.

Effect of Combined and Separated Alloying with Iron and Calcium on the Microstructure and Hardening of Al-8%Zn-3%Mg Alloy

Pavel Shurkin[1], Nikolay Belov[1], Torgom Akopyan[1, 2], Askar Musin[1]

[1]NUST «MISIS», Russia

[2]Baikov Institute of Metallurgy and Material Science, Russia

Abstract. Separated and combined addition of 1 wt. % Ca and 0,5 wt. % Fe to Al-8%Zn-3%Mg alloy was considered in the context of structure and properties relationship. Thermodynamic calculation in the Thermo-Calc software and direct thermal analysis qualitatively provided to predict the phase composition and phase transformations temperatures. With progressive alloying there is a progressive formation of eutectic-formed aluminum-based intermetallics occurs: T phase ($Al_2Mg_3Zn_3$) in the base alloy, $T+Al_3Fe$ in alloy with 0,5 wt. %Fe, $T+(Al, Zn)_4Ca$ in alloy with 1 wt. %Ca and $T+(Al, Zn)_4Ca+Al_{10}CaFe_2$ in alloy with 1 wt. % Ca and 0,5 wt. % Fe. The last ternary phase is attracting the most interest due to its resulted fine morphology unusual for Fe-rich phases. The combination of calcium and iron contributes to grain modifying and hardness increasing after ageing in comparison with the alloys with only Fe and Ca. But at the same time the iron addition leads to lower corrosion resistant which is the same as resistant of basic alloy Al-8%Zn-3%Mg, but higher than resistant of alloy Al-8%Zn-3%Mg-0,5%Fe. The calcium addition allows to significantly decrease Zn/Mg atomic ratio and the iron make it a little higher but it seems not to have influence on the formation to be the main hardening precipitates to be T' phase, which uniformly distributes in the aluminum matrix.

Keywords: Al-Zn-Mg alloy, microstructure, phases, heat treatment, hardness, calcium, iron, alloying elements

1.   Introduction

The approach to design of new aluminum alloys is an important issue in modern material science. As for alloys with increased strength (both cast and wrought) the key point is a formation of structure, morphology and distribution of phases for both equilibrium and non-equilibrium origin.

Aluminum alloys with Zn and Mg are middle strength and able to be welded alloys, which belong to 7xxx type [1-3]. They are widely used in different engineering applications. At the same time the strength of such alloys does not exceed 400 MPa and the latest researches tend not to consider the iron content due to its high limitation [3-5]. According to preliminary research [6] even the 0,3 wt.% of iron make Al-Zn-Mg alloys more anodic and increase the pitting tendency respectively.

There are plenty of works which study the modifications of Fe rich phases. The most iron-containing alloys are cast alloys based on Al-Si system [7]. They are the most recycled and the cheapest too. Plate shaped Al_3Fe, β-Al_5FeSi phases sometimes can contribute to easy extracting of casting from die mold and also to block dislocations in the plastic deformation case [8]. But mainly it is struggled by addition of Mn to form the Chinese script shaped phases α- $Al_{15}(Fe ,Mn)_3Si_2$ or $Al_6(FeMn)$ which are much more fine [9-10]. In this context it seems to be promising to develop new recycled alloys related to other systems, for example Al-Zn-Mg. It can be absolutely novel taking into account some recent papers where the expensive Ag addition is considering [4]. So that the increasing of iron content should be increased there without the main properties loss what is the most challenging purpose.

By this way the iron-rich alloys have been causing an interest in NUST MISIS researches where some promising alloys were developed [11-13]. In particular the alloys called high-strength sparingly alloyed nickalins are based on Al-Zn-Mg-Ni-Fe system. It is convenient to consider two systems Al-Zn-Mg and Al-Ni-Fe separately and to form well-known Al_9FeNi phase of eutectic origin which exists in 2618 alloys type (Al-Cu-Mg-Ni-Fe) [14]. Papers [12] and [15] shows that nickalins with more than 0,5 wt.% Fe has high manufacturability as castings with possibility to obtain tensile strength of more than 500 MPa after heat treatment according to T6. One of the most strength cast aluminum alloy is A206 type has a strict limitation of iron content (no more than 0.07 wt.% in A206.0) [16] Also the presence of up to 5 wt. % Cu contribute to increase of solidification range and low castability especially in hot tearing tendency field [17].

Due to the above facts it is possible to develop new cast alloys based on Al-Zn-Mg system with addition of one of eutectic forming elements (Ni, Ca, Ce etc.). These elements can play the same role as manganese joining into fine phases with iron. One of such elements is calcium which can form Al_4Ca phase and was mentioned as an alloying element in Al-Zn-Mg alloys. It was shown by investigation of group of alloys which contain 0-14% Zn, 0-10%Ca and 3%Mg, that dissolving of Zn in this phase is inevitable and there is an $(Al, Zn)_4Ca$ phase occurs [18, 19]. By the way this fact can cause the degradation of mechanical properties. The paper [20] shows that with addition of iron the $Al_{10}CaFe_2$ phase forms illustrating it with structure of slow cooled Al-6%Zn-3%Mg-2%Ca-0.5%Fe alloy. But the real cast structure was not shown this phase. Nevertheless this research shows the positive effect of iron due to decreasing the amount of zinc in equilibrium phases by showing the difference of hardness between the alloys with and without calcium.

The aim of this work is to investigate the Zn-rich alloy Al-8%Zn-3%Mg and show its structure modification with addition of 1 wt.% Ca and 0,5 wt.% of Fe, considering also phase composition, solidification and hardening.

2.   Methods and experiment

We smelted 4 alloys (shown in Table 1) using pure aluminum (99.97% purity), zinc (99.9% purity), magnesium (99.9% purity) and house-made master alloys Al-15%Ca and Al-10%Fe. Melts were carried out in a resistance furnace. We degassed the metal by injection of C_2Cl_6 powder and poured the molten metal at 720-740 ^{o}C into graphite molds. The castings had 15x30x180 mm in size. In this condition the crystallization rate was about 20 K/s.

Table 1 - Chemical composition of experimental alloys

Alloy	Concentrations, wt. %				
	Zn	Mg	Ca	Fe	Al
A1	8	3	0	0	Balance
A2	8	3	0	0.5	Balance
A3	8	3	1	0	Balance
A4	8	3	1	0.5	Balance

The permanent concentrations of main alloying elements zinc and magnesium were chosen to achieve the highest strength and to simulate the strengthening Zn and Mg rich matrix of one of the most strength commercial alloys 7039 alloy (Al-Zn-Mg-Cu). Consecutive alloying with Fe and Ca allows us to investigate the structure changes carefully and show closely the morphology of the key intermetallic phases.

We used Thermo-Calc software TTAL5 Al-Alloys v5.1 [21] to calculate the phase composition and have a notion about a possible structure of experimental alloys. Also it is convenient to choose the annealing temperature by the way. The direct thermal analysis was carried out with using temperature recorder AKTACOM ATT-2006 and chromel-alumel thermocouple to investigate the solidification behavior and compare the obtained transformations temperatures with calculated ones. According to solidus projection shown in paper [20] the experimental alloys start their crystallization with the most favorable formation of the aluminum solid solution (Al).

We defined the weight loss after holding during 24 hours in corrosion solution (58 g/l NaCl + 33% H_2O_2 water solution) by weighing before and after test. The samples for microstructural research were prepared by polishing with diamond suspension and electrochemical etching (6 C_2H_5OH, 1 $HClO_4$, 1 glycerin). To reveal the grain structure we subjected them to oxidation by electrochemical etching in Barker's reagent (48% water solution HBO_4) for 60 s at 18.0 V and watched the samples at polarized light. We measured the grain by size random linear intercept method. We used transmission electron microscopy (TEM, JEM−2100) to reveal hardening precipitates in substructure. The thin foils for TEM were prepared by ion thinning with a PIPS machine. General structure changes and hardening were investigated using optical microscopy (Axio Observer D1m Carl Zeiss) and Vickers hardness measure (DUROLINE MH-6, loading 1 kgs and holding time 10 s). The hardness was measured five times on each sample after solution treatment and ageing at 100, 125,150, 175, 200, 225, 250 ^{o}C with holding for 3 hours.

3.   Results

3.1 Phase composition and transformation temperatures

Solidus projection shown in Figure 1a allows us to figure out the equilibrium phases forming in each alloy from the liquid phase. We took into account the absence of $Al_{10}CaFe_2$ and $(Al, Zn)_4Ca$ phases in the TTAL5 database and decided to designate it additionally in the corrected projection version presented here. The results of direct thermal analysis are expressed by revealed temperatures of liquidus and solidus. The experimental (non-equilibrium) solidus temperatures were determined by building heating curves and we observed and noted peaks which corresponded to transformations temperatures. The calculated ones were defined using Sheil-Goulliver simulation, which is one of the Thermo-Calc functions allowing us to consider non-equilibrium crystallization which is very important due to formation of T phase at 483 ^{o}C playing the strengthening role precipitating during ageing. Experimental temperatures of each alloy highly correspond to calculated ones as it shown in Figure 1b and Figure 1c.

After defining and checking phase transformation temperatures we can carry out the two step homogenizing annealing 450°C (solution heat treatment) + 520 ^{o}C (fragmentation and spheroidization of non-soluble particles). After this treatment the castings were quenched and subjected to ageing.
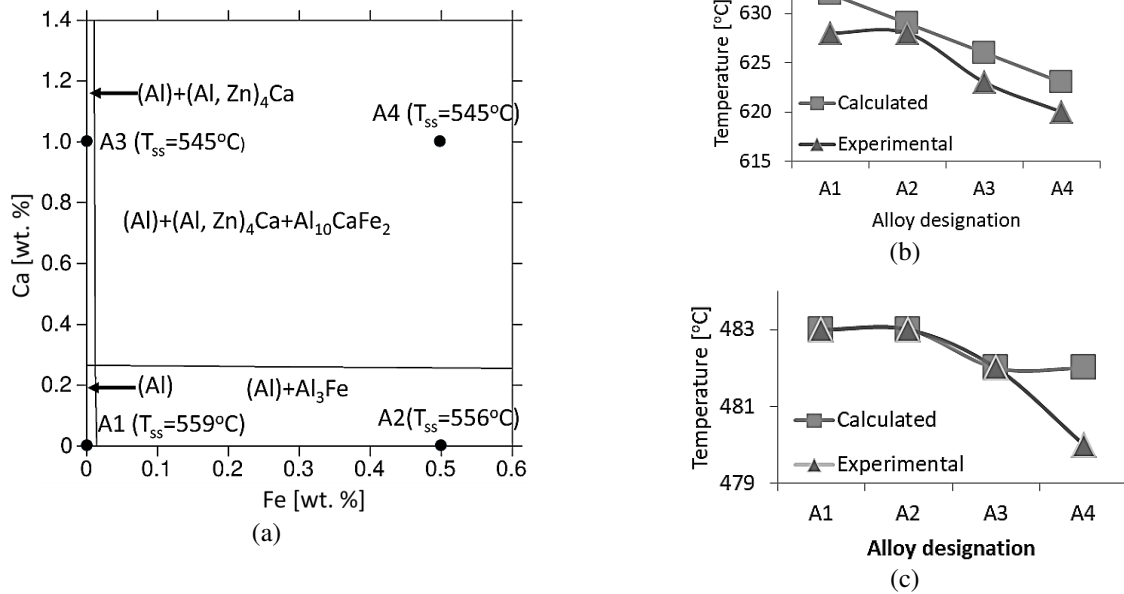
Fig.1. – Calculated (corrected) and experimental results on phase composition and transformations temperatures:
a - solidus projection of Al-8%Zn-3%Mg-Ca-Fe system with indication of experimental alloys position and their equilibrium solidus temperatures (T_{SS}); b – the comparison between calculated and experimental liquidus temperatures; c – the comparison between calculated and experimental solidus temperatures

3.2 Microstructure and morphology of phases

There is an obvious effect of Ca and Fe addition on the grain size as it shown in Figure 2. The base alloy A1 with 8 wt. % Zn and 3 wt. %Mg has the average grain size of 176 μm, and the alloy A4 alloyed with 0,5 wt. % Fe and 1 wt.% Ca has the average grain size of 137 μm. There is no information about calcium effect on the aluminum grain size, but a lot of about positive nucleation effect of iron [22, 23]. Under similar cooling condition it is possible due to formation of Fe-containing phase and foreign particles which both are effective for the nucleation of (Al) and constitutional supercooling.
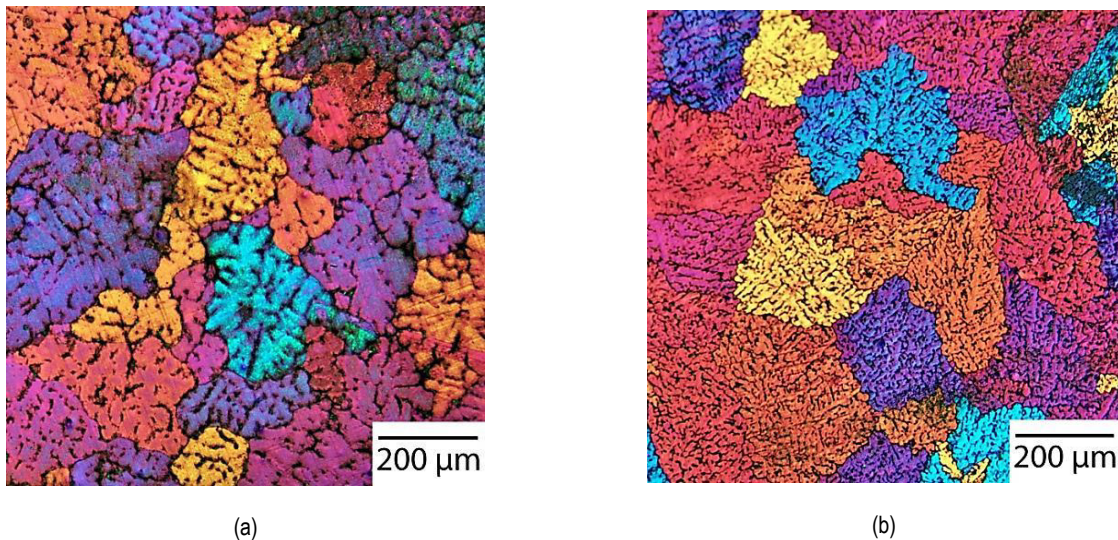
Fig. 2. – Grain structure of alloys: a – A1 alloy; b – A4 alloy

According to the Hall-Patch relation the decrease of grain size leads to improvement of yield strength. Moreover the corrosion rate tended to decrease with decreasing grain size what is a great advantage taking into account the well-known positive effect of calcium what was proved in paper [24]. We defined the weight loss of experimental alloys and confirmed this assumption. Table 2 shows the low corrosion resistance of alloy A2 and the great corrosion resistance of alloy A3. The alloy containing 0,5 wt. % Fe and 1 wt.% of Ca (A4 alloy) shows the same result as alloy A1 which is probably due to $Al_{10}CaFe_2$ formation which is less effective than $(Al, Zn)_4Ca$.

Alloy designation	Entry weight of sample, g	Weight after test, g	Weight loss, %
A1	3,0963	3,0944	-0,0614
A2	3,3601	3,3527	-0,2207
A3	2,7964	2,7963	-0,0036
A4	3,2402	3,2384	-0,0556

The cast structures shown in Figure 3 indicates the modification of Al-8%Zn-3%Mg with addition of 0,5wt.% Fe. The microstructure of the base A1 alloy (Figure 3a) is typical for 7xxx alloys without cooper and contains T phase ($Al_2Mg_3Zn_3$). Some of eutectic are located in the dendritic cells and have the dots shape (Figure 3b). This happened possibly due to partial breakdown of (Al) during one of the crystallization stages.

The T phase has the same morphology in the structure of A2 alloy (Figure 3b). The eutectic formed Al_3Fe is congregated at the junctions of dendritic cells forming the conglomerates with T phase. The amount of T phase veins is much less probably due to higher crystallization rate. Perhaps for the same reason Al_3Fe phase inclusions have not grown to have a coarse plate shape.
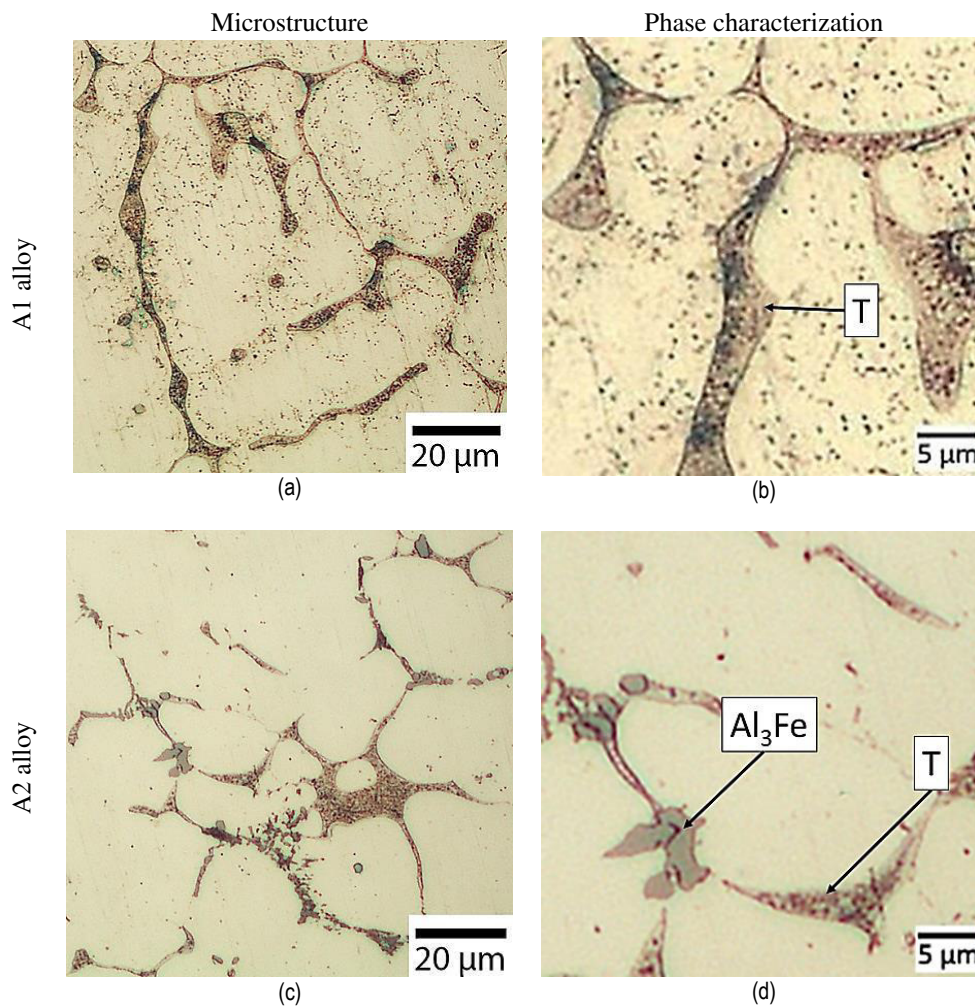
Fig. 3. – As-cast microstructures of experimental alloys A1 and A2

The structure was significantly changed after alloying with calcium. The A3 alloy has a fine structure (Figure 4a) with an eutectic formed (Al, $Zn)_4Ca$ phase and non-equilibrium T phase (Figure 4b) which amount is much less due to Zn solubility in Al_4Ca phase. So that it is expected to have the lowest hardening effect during ageing.

Combined effect of iron and calcium on structure is expressed by both formation of four-component eutectic (Al)+(Al, $Zn)_4Ca+Al_{10}CaFe_2+T$. No traces of Al_3Fe phase were found and an overall microstructure looks favorable (Figure 4c) in comparison with A2 alloy structure. It is possible to define different phases in multiphase structure. As it shown in Figure 4d there are a small plate-shaped (Al, $Zn)_4Ca$ phase, T phase as veins, and Chinese script shaped $Al_{10}CaFe_2$.

	Microstructure	Phase characterization
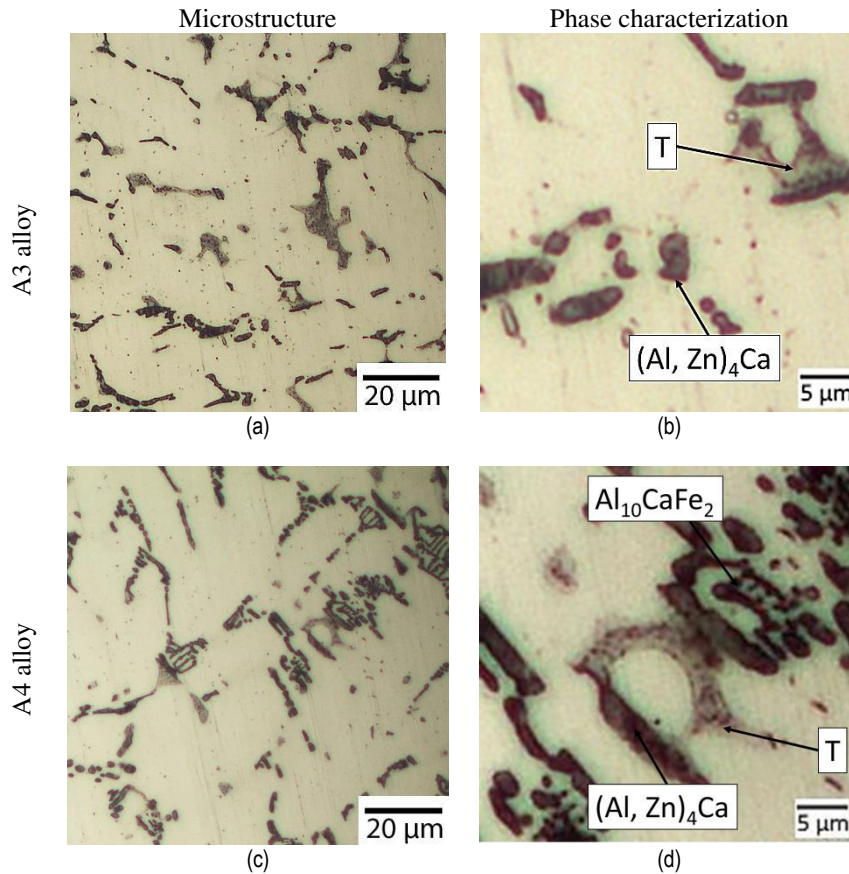
Fig. 4. – As-cast microstructures of experimental alloys A3 and A4

After two-step annealing followed by water quenching the (Al) phase in each experimental alloy should be supersaturated with Zn and Mg. The amount of remained intermetallic particles directly depends on the content of the non-soluble elements Ca and Fe. No primary Fe-rich phases were found in each structure. The A1 alloy has no intermetallics and its structure is not presented here. The remained Al_3Fe inclusions in A2 alloy have not virtually change their shape (Figure 5a). The 1 wt. % Ca containing A3 alloy has fine structure with global-shaped $(Al, Zn)_4Ca$ phase on the boundaries of the (Al) dendritic cells of (Figure 5b). One can observe in A4 alloy the fragmentation and spheroidization of $(Al, Zn)_4Ca$ and $Al_{10}CaFe_2$ phases incorporated in the eutectics (Figure 5c).

In general the structures of A3 and A4 alloys look much favorable to contribute to higher mechanics especially ductility. We suppose that each of experimental alloys can be subjected to high deformation ratio processing, the most likely positive structure would have A4 alloy due to possible uniformly distributed particles of global-shaped $(Al, Zn)_4Ca$ and $Al_{10}CaFe_2$ phases.
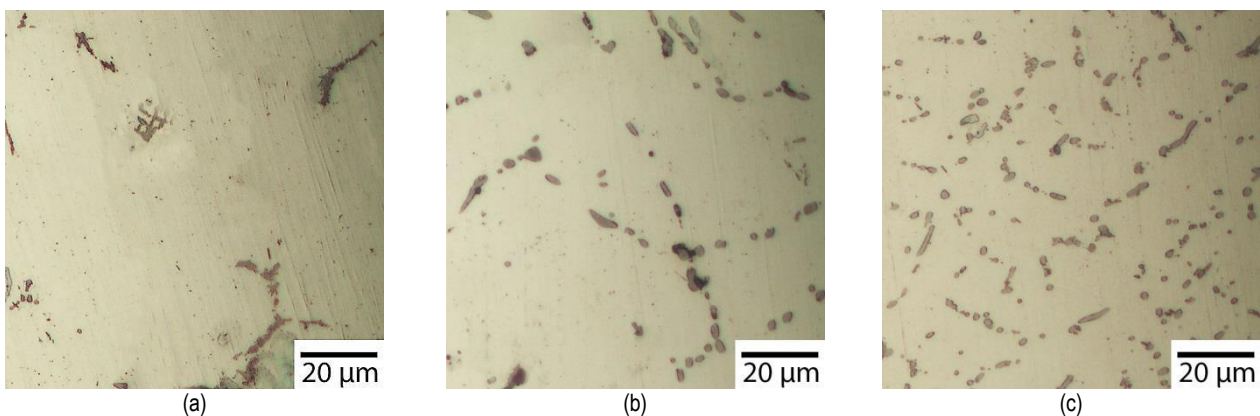

Fig. 5. – Microstructures of experimental alloys after two-step annealing and water quenching: a – A2 alloy; b – A3 alloy; c – A4 alloy

26

3.3 Hardening

The common isothermal sequence is used as: (Al) → Guinier-Preston (GP) zones → metastable η' phase → stable η-phase (MgZn$_2$). Also there can be metastable T' phase to be major hardening precipitates. The type of precipitations depends on Zn/Mg atomic ratio as it described in paper [25]. At Zn/Mg ratio less than 1, the T' phase forms and η' forms at higher ratio. This claim was confirmed in some studies on commercial Al-Zn-Mg alloys [26-28]. The most strength alloys based on Al-Zn-Mg-Cu (7150 type) system have Zn/Mg atomic ratio about 2 and metastable η' phase precipitates there as it shown in [26]. They also confirmed that experimental alloy which contains Al–7.60(3.28)Zn–2.55(2.96)Mg wt.(at.)% is strengthening by T' precipitates. It should be noted that experimental alloys described here is similar to that.

According to calculation on the phase composition at 520 °C in each alloys supersaturated (Al) contains 8.8-8.9 wt.% Zn and 3 wt. % Mg. the volume fraction of T phase is about 35% (in relation to (Al)). It is enough to achieve a quite high level of hardening after ageing. But the existence of (Al, Zn)$_4$Ca phase and Al$_{10}$CaFe$_2$ phase complicates the defining of Zn/Mg ratio in supersaturated (Al). The study [29] showed the EMPA results for the Al-9%Zn-3%Ca-3.5%Mg alloy in as-quenched state. They showed that at this calcium concentration only 4 wt.% Zn remains in supersaturated (Al). Due to this fact we can assume that supersaturated (Al) in experimental alloys A3 and A4 contains more than 6 wt. %Zn and the same content of Mg. Then the Zn/Mg atomic ratio of each alloy is less than 1, what means the T' phase to be the main strengthening precipitates what was also confirmed by calculation of phase composition of (Al) at 175°C which corresponds to maximum hardening (T6) as it shown in fig. 6a. There is a TEM structure presented in fig. 6b which shows a uniform distribution of precipitates, which is possible to be T' phase (fig. 6b). According to cuantity calculation related to (Al) composition the volume fraction of T phase is more than 35%. There are no grain boundaries chains as it sometimes happens in commercial alloys. So that the Ca- Fe- containing alloys can be competitive in the corrosion cracking tendency and ductility after hardening heat treatment at all.

The maximum hardness level was achieved at 175°C and the A1 alloy has the highest hardness level among the all experimental alloys. At low temperatures (100-150 °C) the A2 alloy behaves like the basic one but in T6 condition has 15 units less. Then the alloy with iron is getting absolutely weak as it especially obvious at 200 °C in comparison with A1 alloy. According to hardening curves the A3 alloy with 1 wt. %Ca in after T6 treatment (175 °C , 3h) has a hardness value of 182 HV and with addition of iron it was increased by 10 units (fig. 6a). It proves and confirms the positive effect of calcium on the increasing of zinc content in (Al).So that we assumed that the supersaturated (Al) of A3 alloy contains 6 wt. % Zn and 3 wt.% Mg and the supersaturated (Al) of A4 alloy contains 7 wt. % Zn and 3 wt.% Mg. Perhaps this difference appeared due to Al$_{10}$CaFe$_2$ formation.
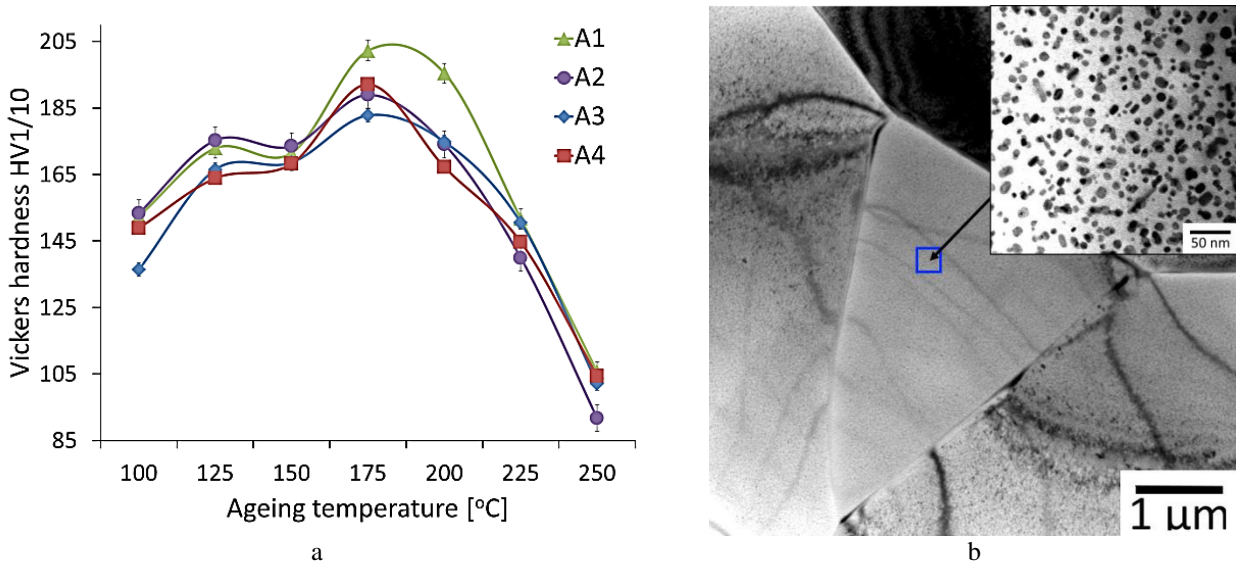
Fig. 6. – Hardening of experimental alloys: a - Hardness as a function of the ageing temperature of experimental alloys; b – TEM structure of A4 alloy after T6 treatment

4.   Conclusions

Using fundamental principles of material science as a composition-structure-properties map there were four experimental alloys investigated. The major conclusions are as follows:

1)   All the alloys compositions contribute to formation eutectic phases of equilibrium and non-equilibrium origin. The liquidus temperature decreases with increasing of alloying level. The possibility of carrying out the spheroidizing annealing at 520 °C was proved.

2)   The efficiency of iron and calcium as grain modifiers was qualitatively shown. Perhaps it can also influence on corrosion resistance. The iron addition to Al-8%Zn-3%Mg alloy significantly increased the weight loss after corrosion test but addition of calcium contributed to return it to have the basic weight loss value.

3)   There are no primary iron-rich phases found. There is a four-component eutectic (Al)+(Al, Zn)$_4$Ca+Al$_{10}$CaFe2+T in alloy containing 0,5 wt. % Fe and 1 wt.% Ca, where all the iron are bounded with aluminum and calcium into compact Chinese script-shaped intermetallics. All of them were fragmentized and spheroidized after two-step annealing to get a fine favorable structure.

4)   Experimental alloys demonstrated significant hardening effect during ageing. According to T6 regime the most strength alloy is a basic one which hardness is 204 HV. The hardness value of 190 HV of A4 alloy with 0,5 wt. % Fe and 1 wt.% Ca is 15 units higher than the hardness of A3 alloy. The results confirmed the positive effect of iron on the precipitates amount which were uniformly distributed in (Al) and were possible to be T' phase.

Acknowledgements

References

[1]   Heinz A., Haszler A., Keidel C., Moldenhauer S., R. Benedictus R., Miller W.S. Recent development in aluminium alloys for aerospace applications // Mater. Sci. Eng. A, Vol. 280, 2000. - p. 102-107.

[2]   Hatch, J.E. (Ed.) Aluminum: Properties and Physical Metallurgy; ASM International: Materials Park, OH, USA, 1984. - 396 p.

[3]   Songyi Chen, Jiyu Li, Gui-yun Hu, Kanghua Chen, Lanping Huang.Effect of Zn/Mg ratios on SCC, electrochemical corrosion properties and microstructure of Al-Zn-Mg alloy // Journal of Alloys and Compounds, Vol. 757, 2018. - p. 259-264

[4]   Lianghua Lin, Zhiyi Liu, Wenjuan Liu, Yaru Zhou, Tiantian Huang. Effects of Ag addition on precipitation and fatigue crack propagation behavior of a medium-strength Al–Zn–Mg alloy // Journal of Materials Science & Technolog, Vol. 34, 2018. – p. 534–540

[5]   Ercan Karaköse, Ali Mawlood Ibrahim, Mustafa Keskın. The Morphological Properties and Microhardness of As-Cast and Melt Spun Al–5Zn–2.5Mg Alloy // Journal of Inorganic and Organometallic Polymers and Materials, Vol. 28, 2018. – p. 2645-2652

[6]   Benedetti A.V., Cabot P.L., Garrido J.A., Moreira A.H. Infuence of iron addition on the microstructure and the electrochemical corrosion of Al-Zn-Mg alloys // Journal of Applied Electrochemistry, Vol. 31, 2001.- p. 293-300

[7]   Zolotorevskiy V. S., Belov N. A. Metal science of casting aluminium alloys, Moscow: MISiS, 2005. 376 p.

[8]   Ceschini L., Boromei I., Morri A., Seifeddine S., and Svensson I.L. Effect of Fe content and microstructural features on the tensile and fatigue properties of the Al-Si10-Cu2 alloy // Materials and Design, Vol. 36, 2012. - p. 522-528

[9]   Anton Bjurenstedt, Daniele Casari, Salem Seifeddine, Ragnvald H. Mathiesen, Arne K. Dahle. In-situ study of morphology and growth of primary α-Al(FeMnCr)Si intermetallics in an Al-Si alloy // Acta Materialia, Vol. 130, 2017. – p. 1-9

[10]   Bo Lin, Rui Xu, Haoyu Li & Weiwen Zhang. Formation of Fe-rich intermetallics in Al–5.0Cu–0.5Fe alloys with different Mn additions // Materials Science and Technology,Vol. 34, Issue 12, 2018. – p. 1447-1459.

[11]   Belov, N. A. Naumova, E.A. Ilyukhin, V. D. Doroshenko, V. V. Structure and mechanical properties of Al – 6% Ca – 1% Fe alloy foundry goods, obtained by die casting // Tsvetnye Metally (Non-ferrous metals), Vol. 3, 2017. - p. 69-75

[12]   Belov N. A., Belov V. D., Alabin A. N., Mishurov S. S. New generation of economically alloyed aluminum alloys // Metallurgist, Vol. 54, 2010. – p. 311-316

[13]   Belov N. A., Alabin A.N., Sannikov A. V., Deev V. B., Tabachkova N. Yu. Effect of Annealing on the Structure and Hardening of Heat-Resistant Castable Aluminum Alloy AN2ZhMts // Metal Science and Heat Treatment, Vol. 56, 2014. – p. 353-358

[14]   Oguocha I., Yannacopolos S. The structure of AlxFeNi phase in Al–Cu–Mg–Fe–Ni Alloy (AA2618) // J Mater Sci, Vol. 9, 1996. - p. 5615-5618

[15]   Shurkin P. K., Akopyan T. K., Korotkova N.O. Influence of hot isostatic pressing on structure and mechanical properties of castings made of high-strength sparingly alloyed aluminium alloy ATs6N0.5Zh (АФ6Н0,5) with increased content of lead // Tsvetnye Metally (Non-ferrous metals), Vol. 9, 2016. - p. 89-96

[16]   The Aluminum Association: Designations and Chemical Composition Limits for Aluminum Alloys in the Form of Castings and Ingot, Washington, DC, 2006.

[17]   Akhyar H., Malau V., Suyitno, Iswanto P.T. Hot tearing susceptibility of aluminum alloys using CRCM-Horizontal mold // Results in Physics, Vol. 7, 2017. - p. 1030-1039

[18]   Belov N. A., Naumova E.A., Akopyan T.K.. Eutectic alloys based on the Al–Zn–Mg–Ca system: microstructure, phase composition and hardening // Materials Science and Technology, Vol. 33, Issue 6. 2017. - p. 656 – 666

[19]   Naumova E.A. Use of Calcium in Alloys: From Modifying to Alloying // Russian Journal of Non-Ferrous Metals, Vol. 59, No. 3, 2018. - p. 284–298

[20]   Shurkin P. K., Dolbachev A.P., Naumova E.A., Doroshenko V.V. Effect of iron on the structure, hardening and physical properties of the alloys of the Al – Zn – Mg – Ca system // Tsvetnye Metally (Non-ferrous metals), Vol. 5, 2018. - p. 69-77

[21]   Thermo-Calc Software TTAL5 Al-Alloys. URL: www.thermocalc.com (access date: 05.12.2018)

[22]   Zhang Y, Ma N, Yi H, et al. Effect of Fe on grain refinement of commercial purity aluminum // Mater Des, Vol. 27, 2006. - p. 794-798.

[23]   Zhang Y., Wang H., Ma N., et al. Effect of Fe on grain refining of pure aluminum refined by Al5TiB master alloy // Mater Lett, Vol. 59, 2005. – p. 3398-3401.

[24]   Volkova O.V., Dub A.B., Rakoch A.G., Gladkova A.A., Samoshina M.E. Comparison of pittong corrosion tendency for castings made of Al_6Ca, Al1Fe, Al_6Ca1Fe experimental alloys and AK12M2 industrial alloy // Izvestiya Vuzov Tsvetnaya Metallurgiya (Proceedings of Higher Schools Nonferrous Metallurgy), Vol. 5, 2017.-p. 75-81.

[25]   Masatomo Nishi, Kenji Matsuda, Naoya Miura, Katsumi Watanabe, Susumu Ikeno, Tomoo Yoshida, Satoshi Murakami. Effect of the Zn/Mg ratio on microstructure and mechanical properties in Al-Zn-Mg alloys // Materials Science Forum, Vols. 794-796, 2014.- p. 479-482.

[26]   Yang X.B., Chena J.H., Liu J.Z., Qin F., Xie J., Wu C.L. A high-strength AlZnMg alloy hardened by the T-phase precipitates // Journal of Alloys and Compounds, Vol. 610, 2014.-p.69-73.

[27]   Liu J.Z., Chen J.H., Yang X.B., Ren S., Wu C.L., Xub H.Y., Zou J. Revisiting the precipitation sequence in Al–Zn–Mg-based alloys by high-resolution transmission electron microscopy // Scripta Materialia, Vol. 63, 2010. - p. 1061–1064.

[28]   Gang Sha, Alfred Cerezo. Early-stage precipitation in Al–Zn–Mg–Cu alloy (7050) // Acta Materialia, Vol. 52, Issue 15, 2004.-p. 4503-4516.

[29]   Belov N.A., Naumova E.A., Akopyan T.K. Effect of Calcium on Structure, Phase Composition and Hardening of Al-Zn-Mg Alloys Containing up to 12wt.%Zn // Materials Research,Vol. 18 , Issue 6, 2015. - p. 1384 – 1391.

Nitrogen Doped Multiwall Carbon Nanotube Sheets as Enhanced-Performance Electrodes in Dye Sensitized Solar Cells

Zharkynay Kuanyshbekova [1,2], Jeliza Bonso [1], Darkhan Ybyraiymkul [2], Ali Aliev [1], and Dauletkhan Smagulov [2]

[1] Alan G. MacDiarmid NanoTech Institute, The University of Texas at Dallas, USA

[2] Kazakh National Research Technical University after K.I.Satpaev, Kazakhstan

Abstract. Catalytic, highly oriented nitrogen-doped multiwalled carbon nanotube (N-doped MWNT) sheets were tested for the electrochemical reduction of triiodide (I_3^-) in dye-sensitized solar cells (DSSCs). Counter electrodes made by stacking multiple N-doped MWNT sheets exhibited better performances than their counterparts made of undoped, pristine MWNT sheets and demonstrated power conversion efficiencies of up to 8%. We foresee that the use of low-density and flexible carbon nanotube aerogel electrodes will be particularly useful in producing flexible, platinum-free DSSC device architectures suitable for electronic textiles.

Keywords: carbon nanotube, dye-sensitized solar cells, counter electrode.

1.   Introduction

Dye sensitized solar cells (DSSCs) have gained much attention as an attractive option for low-cost solar energy conversion, with relatively high efficiency at low embodied energy cost [1, 2]. In a typical DSSC, light is absorbed by a photosensitive dye deposited on a mesoporous titanium oxide (TiO_2) layer that acts as photoanode and working electrode (WE). An electrolyte containing the iodide (I^-)/triiodide (I_3^-) redox couple regenerates the dye by oxidation of iodide at the WE, the produced triiodide then electro-migrates to the counter electrode (CE) where reduces back to its original state, thus completing the overall reaction. The best performing counter electrodes used in DSSCs to date [3] are transparent, conductive oxide (TCO) materials that have catalytic platinum deposited on their surface. The well-known catalytic activity of platinum and its high resistance to corrosion make it essential for the long term operation of dye sensitized solar cells [4]. Nevertheless, the broader use of precious metals such as platinum in daily applications will always be hindered by their scarcity.

While the required quantity of solid platinum loading for the optimal performance of a dye sensitized solar cell is small, some of it is lost through dissolution during cell operation due to the corrosive nature of the electrolyte medium. Thus, current research is focused on the development of alternative counter-electrode catalytic materials that are cost-effective with a close performance to Pt structures [5-7]. Materials such as tungsten oxide [8], cobalt-sulfur compounds [9], and polymer composites [10] have been proposed as plausible candidates to replace platinum in CEs of DSSCs; however most of the latest efforts focus on using different forms of carbon-based materials instead [11-15], since they exhibit less corrosion-related issues during their continuously exposition to the iodide/triiodide redox couple [16-22].

Nitrogen doping of carbon nanotubes (MWNTs) changes their original properties in several ways. For example, certain nitrogen-sites in doped carbon nanostructures can act as n-type dopants and thus increase their electrical conductivity [22]. N-doping also enhances the catalytic behavior of carbon materials for various chemical reactions, like the catalytic splitting of water [23]. In a similar way to these reports, we observed that N-doping of highly porous inverted carbon opals resulted into structures with increased sensitivities towards certain chemical species in gas phase, thus enabling the construction of improved performance gas sensors [24].

The above observations suggest that N-doped carbon nanomaterials, and specifically N-doped MWNTs, could be a suitable catalytic alternative to platinum in the construction of CEs for DSSCs. In this paper, we provide a performance analysis of carbon-based cathode materials made from dry spun sheets of preferentially aligned MWNTs that were doped with nitrogen by a previously reported post-synthesis method [25]. These as produced N-doped MWNTs exhibit an improved catalytic behavior in the electrochemical reduction of triiodide respect to undoped MWNTs, which is likely a result of the higher local positive charge density exhibited by the carbon atoms surrounding the more electronegative N atom dopant [25].

In our previous work [26], we reported the attainment of power conversion efficiencies comparable to the achieved in regular, Pt-based DSSCs by using CEs made of multiple (up to 20) layers of MWNT sheets stacked parallel upon each other. In this work, however, we demonstrate that similar power conversion efficiencies can be obtained using only one quarter of the original MWNT material if we dope our MWNT sheets with nitrogen and use them as CE.

2.   Experimental

2.1 Working electrode

Fluorinated tin oxide glass (SnO_2:F, FTO glass, 8 Ω/□, Hartford Glass) was cut into 1.5 cm^2 rectangular pieces and cleaned in successive baths of deionized (DI) water, ethanol ($_{C2H5OH}$), acetone (($CH_3)_2CO$), and toluene ($C_6H_5CH_3$) for 15 minutes each. The substrates were subsequently exposed to UV radiation for 15 minutes to remove any organic

residue that might remain residues on their surface. After cleaning, these substrates were immersed for 30 min into a 40 mM aqueous solution of TiCl$_4$ at 70ºC, which is a well-established technique for improving the efficiency of dye solar cells [27]. A TiO$_2$ active layer (Dyesol NR-18) was then doctor bladed onto the FTO plate surface to a thickness of approximately 10 μm and then dried in air at 100ºC for 15 min. Next, a second layer (DSL 18NR-AO) was similarly doctor bladed on top of the previously obtained transparent active layer, and dried at 100ºC for 10 min. This bi-layer was sintered for 30 min at 500ºC in air inside a ceramic furnace. After sintering, the FTO substrates were immersed in a clean 40 mM aqueous TiCl$_4$ solution and kept at 70ºC for 30 min. After cleaning in DI water, the substrates were then sintered for a second time at 500ºC for 30 min. Substrates were left to cool to 80ºC before immersing them into a solution 2.52×10-4 M cis-diisothiocyanato-bis(2,2'-bipyridyl-4,4'-dicarboxylato) ruthenium(II) bis(tetrabutylammonium), known as N719 dye (Solaronix) dissolved in 1:1 (v/v) mixture of acetonitrile (C$_2$HN) and tert-butanol ((CH$_3$)$_3$COH).

2.2 Counter electrode

A single ~0.5 mm diameter hole was drilled in each cut FTO coated plates for electrolyte insertion. After drilling, the substrates were cleaned in a similar fashion to the WEs. Dry drawn, preferentially oriented N-doped MWNT sheets were then transferred on top of the hollowed cleansed FTO plates by a technique reported elsewhere [28]. For comparison purposes, conventional platinum electrodes were also prepared by depositing a commercially available hydrogen hexachloroplatinate (IV) solution (HHS) dissolved to a 1:25 (v/v) ratio in isopropyl alcohol (IPA, C$_3$H$_8$O) on the top of a FTO glass substrate. After the platinum precursor deposition, the substrates were annealed in air at 400ºC for 25 min.

2.3   Synthesis of drawable MWNT forests and nitrogen-doping

Iron coated silicon substrates were placed inside a 3 inch quartz tube furnace, which was evacuated and flushed 3 times with helium (He), in order to achieve an inert atmosphere suitable for carbon nanotube growth. The furnace was then heated to 750ºC under continuous He flow. Next, acetylene (C$_2$H$_2$) and hydrogen (H$_2$) were injected inside the quartz chamber to promote carbon nanotube growth by chemical vapor deposition (CVD). After growth time of 6-12 minutes, both, acetylene and hydrogen flows were stopped and the system was allowed to cool to room temperature by natural convection. The collected substrates after CVD are ready for immediate dry sheet drawing of undoped MWNTs.

Nitrogen-doped MWNTs were subsequently obtained by exposing stacks of free-standing, undoped MWNT sheets to a NH$_3$ (0.9 v%)/He plasma for 10 min (100 W, RF source, PT = 900 mtorr) as described in a previous paper [25]. The achieved N-dopant content (N/C atomic ratio) on the MWNTs after this process is typically around 2.1 at% according to X-ray photospectroscopy (XPS) measurements, as shown in Figure 1. During analysis, a binding energy (BE) of 284.6 eV was used as reference value for the C 1s transition in MWNTs [29]. To compute the total atomic ratio of nitrogen, N/C, the measured N 1s and C 1s peaks were fitted using Voigt curves with a Shirley background. The intensities of these curves were then integrated and weighted by their respective sensitivity factor to obtain the atomic abundances of each chemical specie.
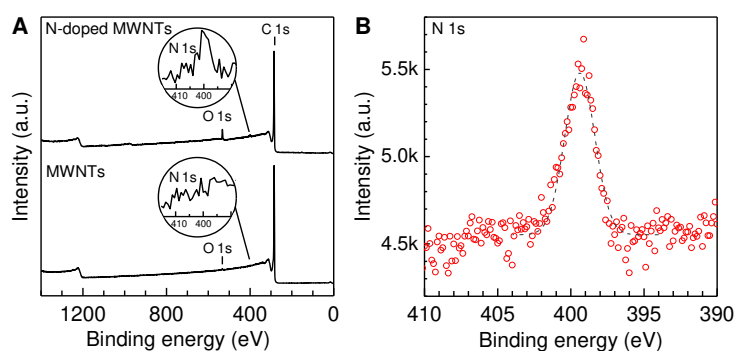

Fig.1. - XPS of MWNTs. (**A**) XPS survey scans of MWNT sheets before and after the N-doping plasma treatment showing a clear evolution of the N 1s peak. (**B**) Higher resolution scans for the N 1s region in N-doped MWNTs. The dashed line shows the obtained fitted curve

2.4. Impedance analysis and solar cell fabrication

Impedance analysis of the nanotube sheets counter electrodes were performed on thin-layer, symmetric dummy cells fabricated by stacking one layer of N-doped (d) with either 1 or 2 layers of undoped (u) MWNT sheets into different configurations (i.e. 1-u/1-d, 1-d/2-u, etc.) until a total of no more than 3 stacked layers. Identical electrodes were sandwiched with a 60 μm-thick Surlyn polymer foil spacer and sealed in a hot press. Control cells made with platinum electrodes were prepared in a similar way but used a 25 μm-thick Surlyn polymer foil as spacer instead. The interelectrode space was filled with a liquid electrolyte consisting of 1-methyl-3-propylimidazolium iodide (0.6 M),

iodine (0.03 M), guanidinium thiocyanate (0.1 M), and 4-tert-butylpyridine (0.5 M) in acetonitrile. All chemicals were purchased from Sigma-Aldrich and used without any further purification. The electrochemical impedance spectroscopy (EIS) measurements were carried out under operating conditions (solar illumination) with zero applied bias over the range of 106-10-2 Hz with a 10 mV AC amplitude in a PGZ 301 potentiostat/galvanostat/EIS.

To prepare the solar cells, the sensitized TiO_2 working electrodes were rinsed with ethanol to remove excess of unabsorbed dye molecules. After drying with nitrogen, TiO_2 WEs were matched with their respective CE of either N-doped MWNTs, pristine MWNTs or Pt and assembled into a cell for testing. The same type of organic electrolyte used for symmetrical cells was introduced into the system via vacuum backfilling through an injection hole in the CE side. After electrolyte filling, the injection hole was sealed with Surlyn resin and a microscope cover glass.

3.   Results and discussion

The demonstrated catalytic efficiency of N-doping MWNT sheets in the oxygen reduction reaction [25], suggests that they could be similarly efficient in other reduction reactions involving a current exchange process, such as the one occurring in the CE of DSSCs.

The N-doping plasma process of MWNT sheets does not significantly changes their overall morphological structure at the microscopic level, as indicated by the SEM shown in Figure 2A-B. Since the main nanotube alignment is conserved and N-doped MWNT sheets remain free-standing after the doping treatment, the DSSC CE construction process can proceed in a similar way to the used for MWNT sheets [26], without need of further modifications. Further examination of individual N-doped MWNTs down to the nanoscale by TEM (Figure 2C-D), reveals that the plasma processing of MWNTs increased their surface roughness by damaging their more external graphitic walls [25] and thus exposing some sections of the inner layers. Such defect generation, heteroatom addition and derived specific area enlargement, are likely responsible of the observed increased power conversion efficiency values exhibited by N-doped MWNTs in DSSCs.
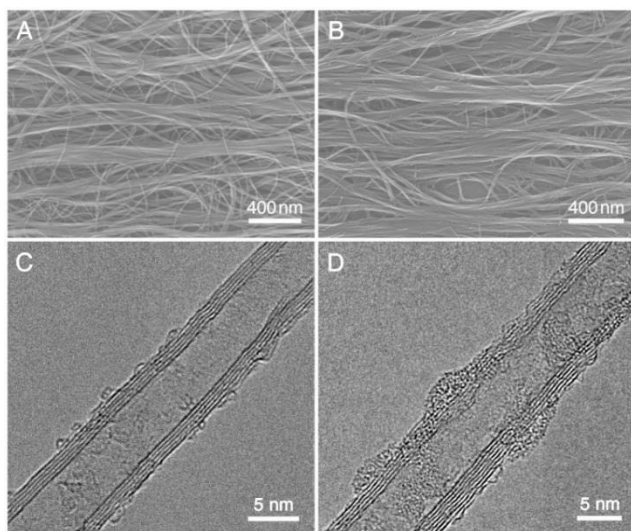
Fig. 2. - Scanning and transmission electron images of (A), (C) undoped and (B), (D) N-doped MWNT sheets

Despite an increment of MWNT sheet resistance by a factor of ~3.3 after doping (Rd/Ru, corrected by a mass loss of 17% due to plasma etching), their charge transfer resistance Rct was reduced according to the EIS measurements shown in Figure 3. Such enhancement could be attributed to the existence of an increased number of sharp atomic edges at the nanotube surface and the addition of N-dopant sites that may play an additional catalytic role for charge transfer.

The Nyquist semicircles recorded for symmetrical cells constructed with N-doped MWNTs in Figure 3 are smaller than those found for cells made using undoped sheets and thus are their exhibited Rct values. This means that the exchange current, which is proportional to the reciprocal of Rct, is larger for N-doped MWNTs. Such improved exchange current value at the CEs is evident by the disappearance of the well-known S-shaped curve typically observed at potentials close to Voc on I-V curves when the charge carrier recombination velocity at the interface is reduced.

Current-voltage performances of DSSCs fabricated with doped and undoped MWNT sheet based CEs recorded under 1 sun illumination (100 mW/cm^2, AM 1.5 G) are compared to those of conventional DSSCs prepared with Pt/FTO CEs in Figure 4. The I-V curve of a CE prepared by stacking 1-layer of N-doped MWNTs over a single undoped MWNT sheet deposited directly on the FTO surface (1d/1u/FTO) show a strong inflection at about 320 mV and 16.8 mA/cm2 (curve 2 in Figure) which is absent in the other stacking configurations: an undoped MWNT single layer on top of a N-doped MWNT single sheet (1u/1d/FTO, curve 3), 1 N-doped layer over 2 undoped MWNT layers (2d/1u/FTO, curve 4) and 2u/1d/FTO (curve 5). The characteristic behavior exhibited by the CE with the 1d/1u/FTO configuration is indicative of insufficient active sites for the triiodide reduction which leads to back reactions and lower filling factors. By simply shifting the CE configuration to 1u/1d/FTO so that now the N-doped MWNTs are in direct

contact with the FTO surface, the above undesired behavior is reversed and a kink-less I-V curve can be obtained, as depicted in curve 3 of Figure . In a similar way, if we increase the effective available area for charge exchange at the interface by just adding one extra undoped MWNT single sheet layer on the CE assembly (and thus increasing the total nanotube areal mass density by about 35%) curves resembling the shape (see 4 and 5 in Figure) of the I-V behavior of Pt/FTO reference electrodes are equally achieved.
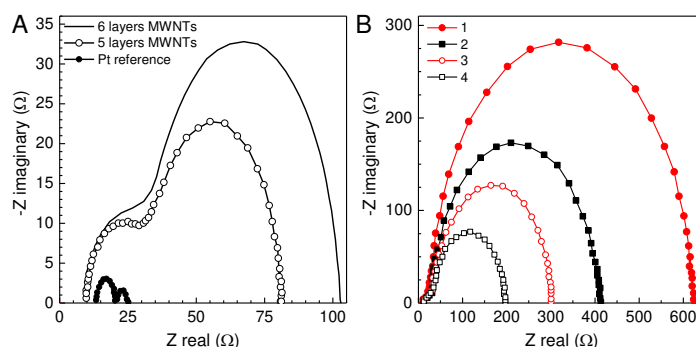

Fig. 3. - Electrochemical impedance spectroscopy of (A) pristine MWNTs and platinum loaded CE as reference, and (B) CE cathodes made of modified carbon undoped (u), and N-doped (d) materials deposited sequentially over the initial FTO surface: (1) 1d/1u/FTO, (2) 1u/1d/FTO, (3) 1d/2u/FTO and (4) 2u/1d/FTO

Measured DSSC parameters, i.e. open-circuit voltage (Voc), short-circuit current density (Jsc), fill factor (FF) and, energy conversion efficiencies (η) for each of the CE configurations tested are summarized in Table 1.

Single MWNT sheet layer CEs exhibit a poor photoelectric performance and high saturation according to their fill factor and conversion efficiency values which is in agreement with our previous work [26]. Given that the electrical resistance of MWNT sheets increases after the N-doping treatment we decided to stack them together with undoped MWNT sheets to compensate for their electrical conductivity loss when assembling the CEs. In this way we were able to take advantage of the enhanced catalytic activity of N-doped MWNTs without sacrificing electrode internal electrical conductivity.

This approach resulted in N-doped/undoped MWNT CEs with close Voc and Jsc values to the exhibited when Pt is used as counter electrode. In fact, relatively high conversion efficiencies of up to 6.26% were attained if one N-doped MWNT sheet was stock on top of 2 sheet layers of undoped MWNTs (1d/2u/FTO) which are just 3.47% below the achieved for Pt/FTO (9.73%)
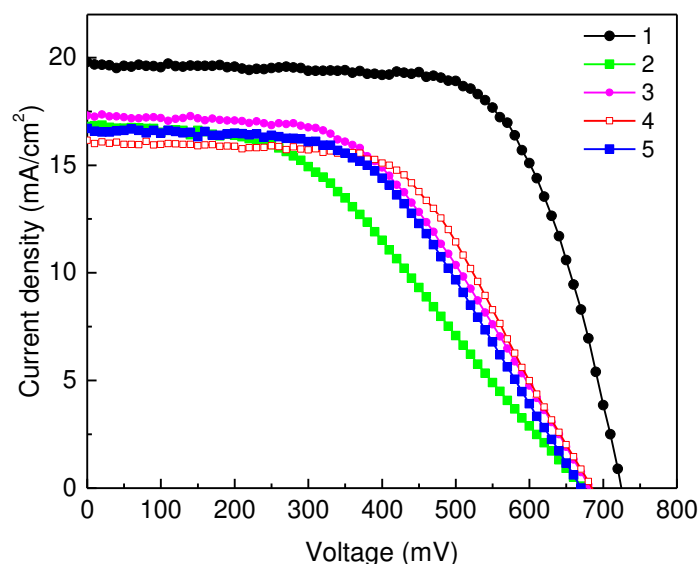
Fig. 4. - Current-voltage characteristic curves of different stacking combinations of MWNT based materials deposited directly on FTO: (1) Pt reference, (2) 1d/1u/FTO, (3) 1u/1d/FTO, (4) 1d/2u/FTO and (5) 2u/1d/FTO

Table 1- Summary chart of DSSC characteristics from the data presented in Figure

№	Counter electrode	V_{oc} (mV)	I_{sc} (mA/cm^2)	FF	η (%)
1	Pt reference	730	19.8	0.67	9.73
2	1d/1u/FTO	680	16.8	0.41	4.72
3	1u/1d/FTO	690	17.3	0.50	5.96
4	1d/2u/FTO	690	16.1	0.56	6.26
5	2u/1d/FTO	680	16.7	0.51	5.77

Next, DSSCs fabricated with CEs comprised of solely N-doped MWNTs were compared with the Pt reference in the same test as depicted in Figure and Table 2 so that discrepancies between batch variations were minimized and comparisons with Pt could be made directly rather than through global averages. Current density-voltage measurements showed that by using only 5 layers of N-doped MWNT sheets stacked on each other, it was possible to reach CE power conversion efficiencies (PCE) of up to 8.86%, just 1% below of their Pt counterparts (see table 2). This contrast with the necessary 20 layers (and ~4.8 times of mass increase) required to achieve a similar effect in CEs made of undoped MWNT sheets [26]. This supports our hypothesis that the catalytic properties of N-doped MWNTs could be exploited beyond the ORR [25] and used for other applications involving the reduction of electroactive species such as in the case of the I-/I3- redox couple in DSSCs.
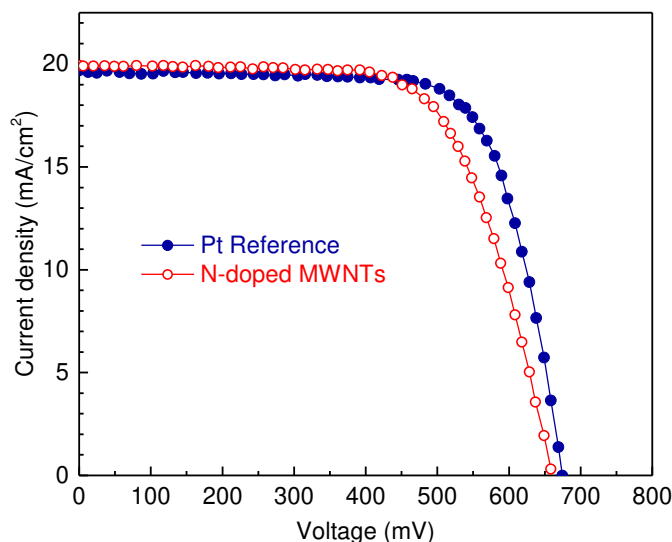

Fig. 5. - Current-Voltage characteristics of DSSC with layered N-doped carbon MWNT and platinum counter-electrodes

Table 2 - Summary chart of DSSC characteristics from the data presented in Figure

Counter electrode	V_{oc}, mV	I_{sc}, mA/cm^2	FF	PCE
Pt Reference	680	19.98	0.73	9.87
N-doped MWNTs	670	19.89	0.67	8.86

4.   Conclusions

Nitrogen doping carbon MWNT sheets is an excellent alternative to produce multilayer carbon DSSCs electrodes with comparable performances to standard Pt-coated CEs. Power conversion efficiencies over 8% can be obtained by using 5 sheet layers of N-doped MWNTs, which is almost 5 times lesser material than the needed of undoped MWNTs to achieve similar efficiency values. This enhanced efficiency is proven to be a consequence of N-doped MWNTs reduced charge transfer resistance and exhibited higher exchange currents, phenomena likely related to the nitrogen-sites presence and increased nanotube surface roughness. We expect that the demonstrated catalytic activity of N-doped MWNTs on the triiodide reduction reaction would allow construction of flexible, platinum-free DSSC electrodes that can be ultimately included in textiles in the near future.

5.   Acknowledgements

References

[1] B. O'Regan and M. Grätzel, Nature 353, 737 (1991).
[2] M. Grätzel, Nature 414, 338 (2001).
[3] A. Yella, H.-W. Lee, H. N. Tsao, C. Yi, A. K. Chandiran, M. K. Nazeeruddin, E. W.-G. Diau, C.-Y. Yeh, S. M. Zakeeruddin, and M. Grätzel, Science 334, 629 (2011).
[4] H. Bönnemann, G. Khelashvili, S. Behrens, A. Hinsch, K. Skupien, and E. Dinjus, Journal of Cluster Science 18, 141 (2007).
[5] X. Fang, T. Ma, G. Guan, M. Akiyama, T. Kida, and E. Abe, Journal of Electroanalytical Chemistry 570, 257 (2004).

[6] E. Olsen, G. Hagen, and S. Eric Lindquist, Solar Energy Materials and Solar Cells 63, 267 (2000).

[7] N. Papageorgiou, Coordination Chemistry Reviews 248, 1421 (2004).

[8] M. Wu, X. Lin, A. Hagfeldt, and T. Ma, Chemical Communications 47, 4535 (2011).

[9] M. Wang, A. M. Anghel, B. Marsan, N.-L. Cevey Ha, N. Pootrakulchote, S. M. Zakeeruddin, and M. Grätzel, Journal of the American Chemical Society 131, 15976 (2009).

[10] B. Fan, X. Mei, K. Sun, and J. Ouyang, Applied Physics Letters 93, 143103 (2008).

[11] A. Kay and M. Grätzel, Solar Energy Materials and Solar Cells 44, 99 (1996).

[12] T. Hino, Y. Ogawa, and N. Kuramoto, Carbon 44, 880 (2006).

[13] E. Ramasamy, W. J. Lee, D. Y. Lee, and J. S. Song, Applied Physics Letters 90, 173103 (2007).

[14] T. N. Murakami, S. Ito, Q. Wang, M. K. Nazeeruddin, T. Bessho, I. Cesar, P. Liska, R. Humphry-Baker, P. Comte, P. Péchy, and M. Grätzel, Journal of The Electrochemical Society 153, A2255 (2006).

[15] E. Ramasamy, W. J. Lee, D. Y. Lee, and J. S. Song, Electrochemistry Communications 10, 1087 (2008).

[16] Z. Huang, X. Liu, K. Li, D. Li, Y. Luo, H. Li, W. Song, L. Chen, and Q. Meng, Electrochemistry Communications 9, 596 (2007).

[17] H. Choi, H. Kim, S. Hwang, W. Choi, and M. Jeon, Solar Energy Materials and Solar Cells 95, 323 (2011).

[18] C.-T. Hsieh, B.-H. Yang, and J.-Y. Lin, Carbon 49, 3092 (2011).

[19] J. G. Nam, Y. J. Park, B. S. Kim, and J. S. Lee, Scripta Materialia 62, 148 (2010).

[20] P. Joshi, L. Zhang, Q. Chen, D. Galipeau, H. Fong, and Q. Qiao, ACS Applied Materials & Interfaces 2, 3572 (2010).

[21] K. Imoto, K. Takahashi, T. Yamaguchi, T. Komura, J.-i. Nakamura, and K. Murata, Solar Energy Materials and Solar Cells 79, 459 (2003).

[22] K. Gong, F. Du, Z. Xia, M. Durstock, and L. Dai, Science 323, 760 (2009).

[23] Y. Zhao, R. Nakamura, K. Kamiya, S. Nakanishi, and K. Hashimoto, Nature Communications 4 (2013).

[24] A.Morelos-Gómez, P. G. Mani-González, A. E. Aliev, E. Muñoz-Sandoval, A. Herrera-Gómez, A. A. Zakhidov, H. Terrones, M. Endo, and M. Terrones, Advanced Functional Materials 24, 2612 (2014).

[25] X. Lepró, R. Ovalle-Robles, M. D. Lima, A. L. Elías, M. Terrones, and R. H. Baughman, Advanced Functional Materials 22, 1069 (2012).

[26] Z. Kuanyshbekova, C. Huynh, S. Hawkins, D. Smagulov, S. Malayev, and A. Zakhidov, Advanced Materials Research 622-623, 833 (2012).

[27] P. M. Sommeling, B. C. O'Regan, R. R. Haswell, H. J. P. Smit, N. J. Bakker, J. J. T. Smits, J. M. Kroon, and J. A. M. van Roosmalen, The Journal of Physical Chemistry B 110, 19191 (2006).

[28] M. Zhang, S. Fang, A. A. Zakhidov, S. B. Lee, A. E. Aliev, C. D. Williams, K. R. Atkinson, and R. H. Baughman, Science 309, 1215 (2005).

[29] T. I. T. Okpalugo, P. Papakonstantinou, H. Murphy, J. McLaughlin, and N. M. D. Brown, Carbon 43, 153 (2005).

The Research of Parameters of Flame Spray Coatings Ni-Cr and Ni-Cr-Wc

Olegas Černašėjus, **Ovidijus Jarašūnas**
Vilnius Gediminas technical university, Lithuania

Abstract: The article deals with flame spray Ni-Cr coatings on structural steel S235 substrate. Before spraying substrate surfaces were processed mechanically. Coatings were sprayed using Ni-Cr and Ni-Cr-WC spray powder of different chemical composition and additional substrate heating up to 250–290°C. Microstructure, porosity, hardness, friction coefficient and wear resistance of created coatings Ni-Cr and Ni-Cr-WC were examined. Influence of coating chemistry and WC carbides on various physical, tribological parameters of coatings was evaluated and dependencies of such coating characteristics were determined.
Key words: thermal spray coatings, Ni-Cr and Ni-Cr-WC, flame spraying, characteristics.

1. Introduction

Thermal spray technique is one of the most effective processes to avoid surface corrosion, oxidation and wear. It is the process when small drops of liquid material melted by concentrated energy source, accelerated and propelled toward the material to be covered (substrate) crystalize and thus produce coating of the surface. By such technique various coatings protecting surface from negative environmental impact and improving their performance characteristics are built. Thermal spray coatings are widely used in aviation, machine production, to restore or to cover transport components, in chemical industry, electronics etc. [1]. Metal alloys, carbides, metal oxides, metal/ceramics compounds may be used by thermal spray technique to cover surface and to create wear, corrosion and oxidation resistant coatings [2].

Flame spraying is one of the oldest and widely used thermal spray techniques. It is technologically straightforward, cheap, compact, universal and mobile process ensuring high productivity and comparatively good coating quality [1]. Spray material may be in powder, wire or a rod form. Production of wire and rod out of some materials is very expensive or even impossible still materials in powder form may be produced of any chemical composition. Thus flame powder spraying process is the mostly used thermal spraying technique which can be used to spray coatings out of wide spectrum of materials. Nickel based coatings are the most favourite of flame spray coatings. Nickel based coatings are effectively used to build wear resistant surfaces in case of corrosion medium and high temperature oxidation [3-4]. Protective nickel based coatings are widely used in different industries due to exceptional properties of nickel itself. Pure nickel is tensile and plastic because it retains cubic centered surface grid up to the melting point (1453°C) consequently transition tensile-brittle is not inherent to nickel alloys. Nickel makes hard solution with many elements. It allows to vary special alloy properties in wide range while changing amount and proportion of alloying elements: to improve mechanical resistance strengthening hard solution, structuring dispersion phases and solid inserts and to improve resistance to corrosion and high temperature oxidation as well. Due to mentioned properties nickel is excellent base for production of protective coatings [5].

In order to improve properties of spray coatings metal carbides (WC, TiC, VC, $B_{13}C_2$, SiC ir kt.), borides (TiB_2), oxides (CeO_2, La_2O_3, Y_2O_3, Al_2O_3 and others) or similar are added to spray powder [6-9]. Research shows that tungsten or other metal carbides foremost have strong effect on mechanical resistance increasing hardness, wear resistance. Due to excellent moistening properties of nickel based matrix tungsten carbides WC are most often used in commercial mixtures. Their presence in the matrix likewise stimulates formation of hard phases such as NiB_3 or M_6C [7, 10-11].

The main goal of the research was to investigate physical and tribological properties such as porosity, hardness, tensile modulus and wear resistance of flame spray Ni-Cr coatings with different chemical composition sprayed on structural steel S235 and to compare properties of Ni-Cr-WC to Ni-Cr ones.

2. Methodology of experimental investigation

Flame spray technique was used to spray coatings on 160 × 30 × 8 mm specimens of structural steel S235. Commercial flame spraying equipment Castolin Eutectic „ROTOTEC 80" was used for the experiment.

Chemical composition of commercially available Ni-Cr based flame spray powder used for the experiment is shown in Table 1.

Table 1 - Chemical composition (in wt. %) of Ni-Cr flame spray powder

Ni	Cr	Si	Fe	Al	C
Base	14-20	4-4.5	3-7	0.8-1.2	0.6-1

Tungsten carbide (WC) powder was added to the commercially available standard powder in different proportions in order to improve physical and operational quality of spray powder. Thus 4 coatings with different chemical composition were obtained: standard Ni-Cr based coating, coating having WC content of 10% WC, coating having WC content of 15% and coating having WC content of 20%. Designation of samples depending on WC content in Ni-Cr coating is presented in Table 2.

Table 2 - Designation of samples

Chemical composition of powder, in %	Sample designation
100Ni-Cr	B0
Ni-Cr + 10WC	B1
Ni-Cr + 15WC	B2
Ni-Cr + 20WC	B3

Before flame spraying Ni-Cr-WC powders was well stirred at n = 60min^{-1} and time span 20 min. Spray powder was dried in electric heater for 30min. at temperature of 350°C.

Before spraying surfaces of all specimens of structural steel S235 were processed by cut wire shot following standard EN 14616. Before spraying structural steel plates were heated by neutral acetylene and oxygen flame up to temperature of 250–290°C when linear heating speed v = 0,046m/min.

The main flame spraying parameters were as follows: stand-off distance 70mm, flame making gases oxygen (4bar) and acetylene (0,6bar), number of spray passes 22, linear spraying speed v = 0,6m/min.

Microstructure of spray coatings was examined observing surfaces of cross microsections of grinded and polished coatings by optical microscope „Nicon Eclipse MA 200". Analysis of microstructure of powder containing tungsten carbide was carried out by scanning electron microscopy equipment SEM JEOL JSM-7600F with secondary electron SE detector enlarging image 200 and 5000 times. The parameters of electron microscopy was as follows: voltage 15 kV, distance to the specimen 14,7 mm.

Porosity of flame spray coatings was examined by microscopic technique using Scion Image software. Images of microstructure obtained by optical microscope were processed by the software using 100 times magnification.

Hardness of various coatings was measured by Rockwell hardness tester in HRB scale using 1,6 mm diameter sphere. Hardness of coatings was recalculated in HV units.

„Ball on plate" testing scheme and 5 mm diameter sphere of zirconium oxide was chosen for the wear resistance test of spray coatings. Dry friction test was chosen for the experiment when duration of one test is 60 min. and number of machine revolutions is n= 200 min^{-1}. Three different loads were used for the test (12,5 N, 11,5 N ir 10,5 N). All tests were carried out following requirements of standard ASTM G-99. Wear resistance was calculated according to mass loss. Electronic analytical scales KERN 770-14 measuring with 0,1 mg precision were used for weighing. After every wear test the plate was cleaned by air flow and ultrasonic equipment to remove all dirtiness. Before wear test the plates were grinded by abrasive grinding machine to reduce influence of roughness on test results. Roughness of grinded specimens was measured by profilometer TR200 and Ra reached 0,7–1,5µm.

The friction coefficient test of sprayed coatings was performed on a Macmesin multitest 2.5-i measuring equipment and using „Plate on plate" testing scheme.

3.   Results and Discussions

Having analyzed Ni-Cr-WC powder by scanning electronic microscope it was found that the spray powder is composed of particles of different form and fraction (Figure 1). Results of X-ray microanalysis has shown that round shape particles are Ni-Cr particles and irregular form particles are WC (Figure 2).

During microscopic examination of flame spray coatings Ni-Cr and Ni-Cr-WC (B0-B3) it was found that sprayed layers of coating have lamellar structure with quite significant coating porosity which is characteristic of flame spray coatings.
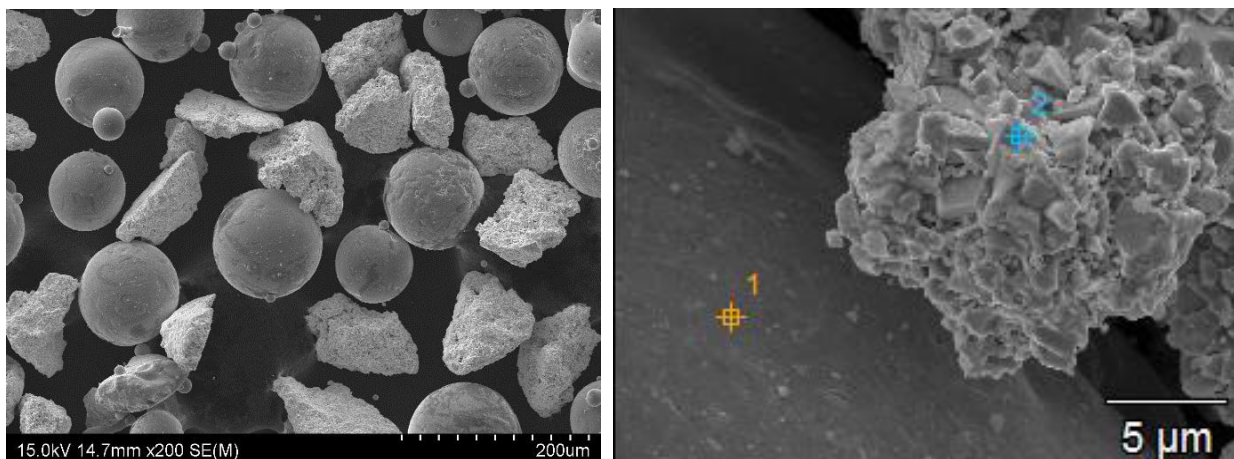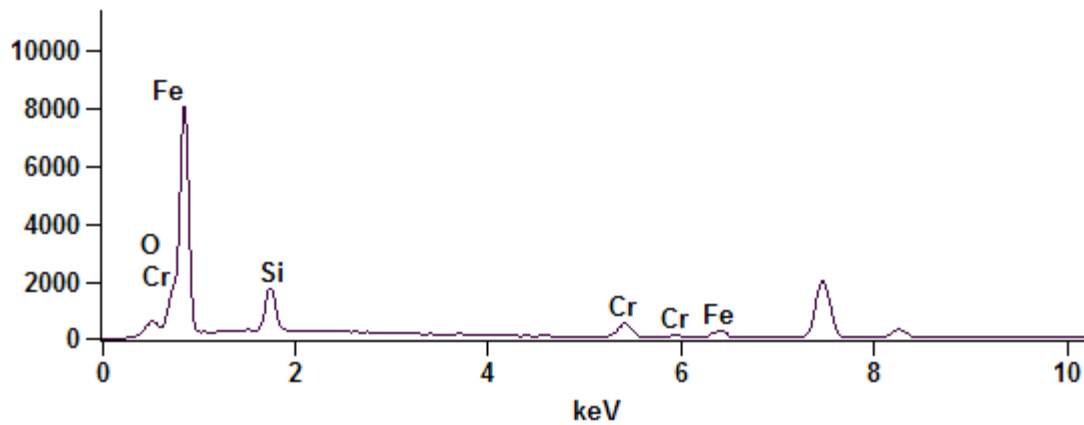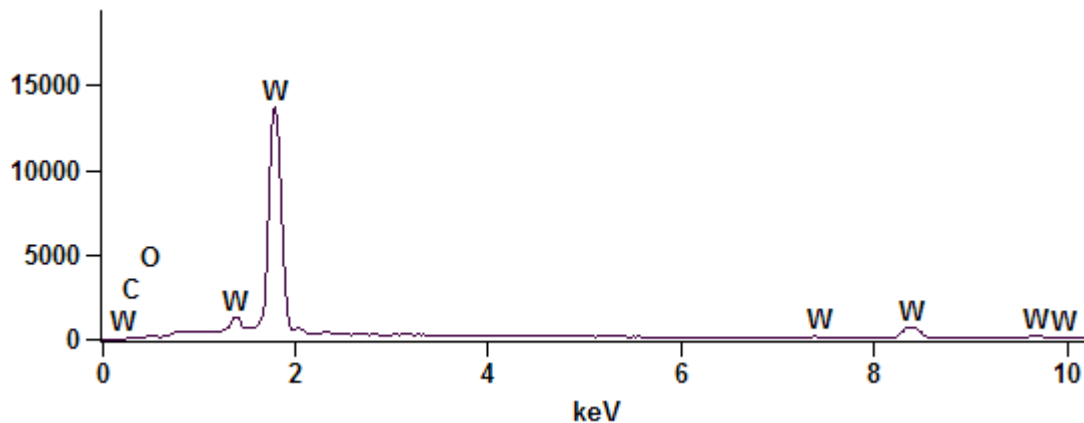

Fig. 1. - Morphology of Ni-Cr-WC flame spraying powder

(a)

(b)

Fig. 2 - The results of X-ray microanalysis of B2 spray powder: a) 1 area; b) 2 area (see Figure1)

Unmelted particles of spray powder keeping their original form were observed in some places of the coating among properly sprayed lamellae.

When analyzing microstructure of Ni-Cr and Ni-Cr-WC coatings it was observed that Ni-Cr coating (B0) without WC is characterized by more homogeneity microstructure consist from hard nickel solution with dispersive carbides (chromium carbide). Contrary to Ni-Cr coatings Ni-Cr-WC coatings (B1–B3) are characteristic of high heterogenity of microstructure.

Porosity of coatings was established analyzing polished cross-section images by „Scion Image" software and expressed as percentage ratio between pores area and whole cross-section area being analyzed. Results of coatings porosity is presented in Table 3.

Table 3 - Porosity of Ni-Cr and Ni-Cr-WC sprayed coatings, %

Measurement	Coatings			
	B0	B1	B2	B3
1	16%	20.7%	18.5%	19.8%
2	10.4%	15.7%	18.8%	23.6%
3	13.9%	18.5%	21.8%	31.3%
4	14.9%	21.7%	23.9%	33.5%
5	17.1%	17.2%	24.5%	20.6%
Average value	14.5%	18.7%	21.5%	25.8%

The analysis has shown that porosity of Ni-Cr coating amounts to 14,5 %. The highest porosity value reaching almost 25,8% was found in Ni-Cr coating with WC content of 20% (B3). The lowest porosity value (18,7%) of Ni-Cr-WC coating was determined in coating having WC content of 10% (B1) Such Ni-Cr-WC coatings (B1–B3) with quite significant porosity may be used for production of wear resistant surfaces at limiting (minimal) lubricating.

Thus during experimental tests Ni-Cr-WC coatings obtained on the surface of specimens were rather heterogeneous with porosity varying from 14,5 to 25,8%. Such superficial pores formed in spongy coatings can fulfil lubricating function in various lubricant media and protect surface from wear.

Dependence of hardness values of coatings Ni-Cr and Ni-Cr-WC on content of tungsten carbide present in the coating is shown in Figure 3.
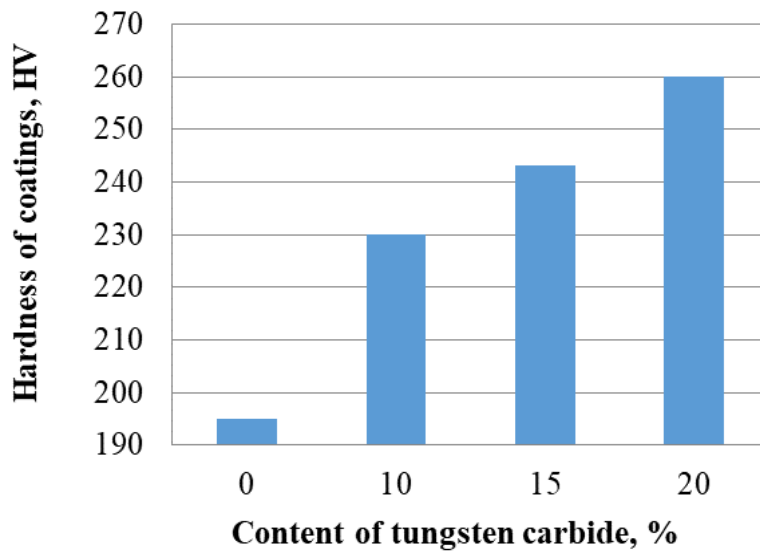

Fig. 3 - Hardness of sprayed coatings B0-B3 dependence from content of tungsten carbide

Wear tests of spray coatings Ni-Cr and Ni-Cr-WC in the air has shown the weight loss of spray specimens at different loads: 12,5N, 11,5N, 10,5N (Figures 4 – 6). The results have shown that at different loads of wear test the highest mass loss was found for Ni-Cr+20WC coating (B3). This could have been determined by high brittleness of the coating and bad adherence of separate particles of the coating. The test results have shown that at load of 12,5N coatings Ni-Cr+10WC and Ni-Cr+15WC (B1 and B2) are more wear resistant than coating Ni-Cr (B0).

The test showed that at load 11,5N coatings Ni-Cr and Ni-Cr+15WC (B0 and B2) were almost equally wear resistant when sliding track was 1000m (Figure 5). However, when sliding track was 2000 m coating Ni-Cr (B0) was less wear resistant than coatings Ni-Cr+10WC and Ni-Cr+15WC (B1 ir B2). Experimental tests of wear resistance have also revealed that coatings Ni-Cr+10WC and Ni-Cr+15WC (B1 and B2) had identical wear resistance and were more wear resistant than coating Ni-Cr (B0) at wear load of 10,5N.
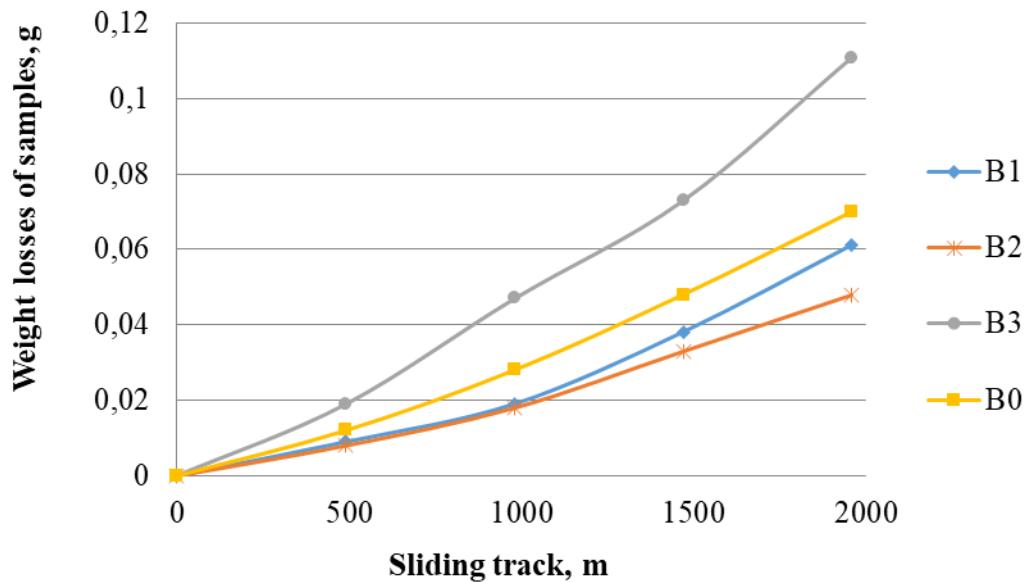

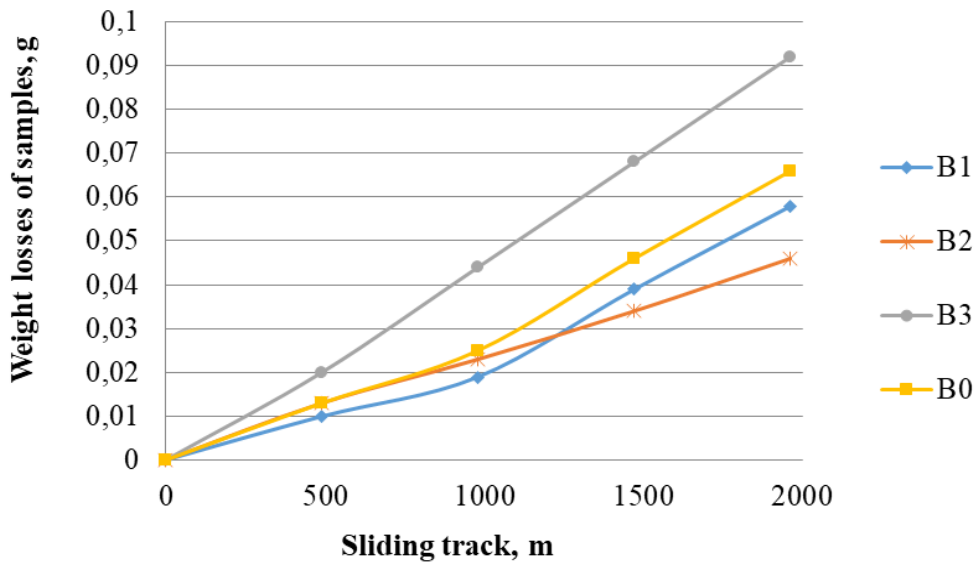**Fig. 4.** - Weight losses of samples, when the load of 12.5N

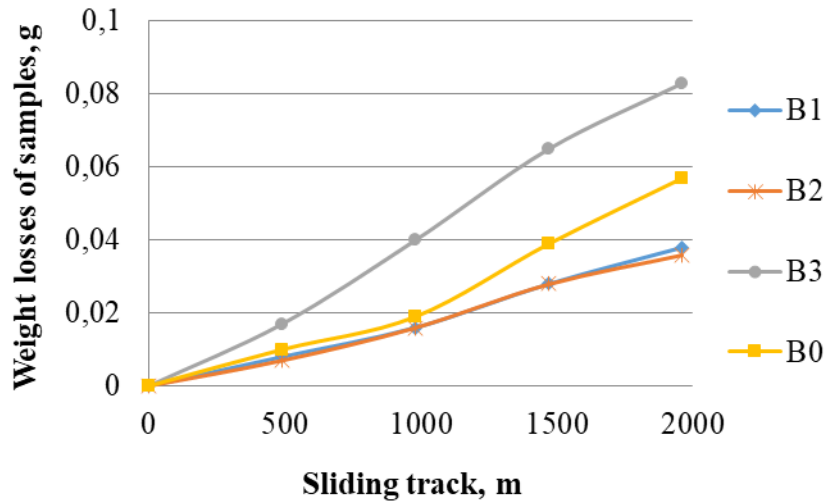**Fig. 5.** - Weight losses of samples, when the load of 11.5N

Fig. 6. - Weight losses of samples, when the load of 10.5N

Tribological test with identical materials in friction pairs has shown the highest friction coefficient of coating B3 and the lowest friction coefficients of coatings B1 and B2 (Table 4). These coatings are the most wear resistant and have the lowest friction coefficient.

Table 4 - Results of a friction test with identical materials in friction pairs

Friction pair	Normal force, N	Friction force, N	Friction coefficient
B1/B1	1.668	0.334	0.200
B2/B2	1.6778	0.338	0.201
B3/B3	1.6307	0.399	0.245
B0/B0	1.7159	0.387	0.225

Tribological test with different materials in friction pairs has shown the highest friction coefficient of friction pair B0/B2 coatings and the lowest friction coefficient of friction pair B1/B0 coatings (Table 5).

Table 5 - Results of a friction test with different materials in friction pairs

Friction pair	Normal force, N	Friction force, N	Friction coefficient
B0/B0	1.7159	0.387	0.225
B1/B0	1.668	0.310	0.186
B2/B0	1.6778	0.413	0.246
B3/B0	1.6307	0.379	0.232

4.   Conclusions

Spray coatings were built on the surface of mechanically processed and heated steel by flame spraying technique using spray powder Ni-Cr and WC of different proportions. Microstructure, porosity, hardness and wear resistance of the coatings were investigated. The received results make it possible to draw the following main conclusions:

1) The experimental study has found that nickel-chromium coatings with tungsten carbide have high hardness and porosity and consequently can be used to make wear resistant surfaces at limiting or minimal lubrication.

2) Metallographic tests have determined that fusion lines of spray coatings Ni-Cr and Ni-Cr-WC were without gaps however the coatings had high porosity. The lowest coating porosity was in nickel-chromium coating (14,5%) and coating with tungsten carbide content of 10% (18,7%). The highest porosity was in coatings with tungsten carbide content of 20% and reached 25,8%.

3) Addition of tungsten carbide to nickel-chromium flame spray powder has great influence on general hardness of the coating. The test has shown that the highest hardness of the coating (260HV) was achieved with the coating having tungsten carbide content of 20%.

4) Wear resistance test has shown that the coating having tungsten carbide content of 15% was the most wear resistant and nickel-chromium coating and nickel-chromium coating having tungsten carbide content of 20% was the least wear resistant. Coating having tungsten carbide content of 10% had slightly different wear resistance from coating having tungsten carbide content of 15%.

5) Friction coefficients were measured for all coatings by friction coefficient testing. During friction test with identical materials the lowest friction coefficient of $\mu = 0,200$ was found for coating having tungsten carbide content of 10% and the highest friction coefficient of $\mu = 0,245$ was found for coating having tungsten carbide content of 20%. During friction test with different materials the lowest friction coefficient of $\mu = 0,186$ was found for coating having tungsten carbide content of 10% and the highest friction coefficient of $\mu = 0,246$ was found for coating having tungsten carbide content of 15%.

6) Investigation of physical and tribological properties of nickel-chromium flame spray coatings having tungsten carbide has found that the optimal tungsten carbide content is 10%.

References

[1] Davis J. R. Handbook of thermal spray technology. Materials Park (Ohio): ASM International, 2009. - 338 p.

[2] Dorfman M.R. Thermal spray coatings. Handbook of Environmental Degradation of Materials, 2nd ed., 2012. – p.569–596.

[3] Yu H.L., et al. Comparison of surface and cross-sectional micro-nano mechanical properties of flame sparyed NiCrBSi coating //Journal of Alloys and Compounds, 672, 2016. – p. 137–146.

[4] Dong S., *et al*. Deposition of NiCrBSi coatings by atmospheric plasma spraying and dry-ice blasting: Microstructure and wear resistance //Surface and Coatings Technology, 268, 2015. - 36–45.

[5] Davis J.R.. Nickel, cobalt and their alloys. ASM Specialty Handbook. Materials Park : ASM International,2000. - 442 p.

[6] Cai B., et al.. Tribological behavior and mechanism of NiCrBSi–Y_2O_3 composite coatings // Transactions of Nonferrous Metals Society of China, 23, 2013. - p. 2002–2010.

[7] Serres N., et al. Microstructures and mechanical properties of metallic NiCrBSi and composite NiCrBSi–WC layers manufactured via hybrid plasma/laser process //Applied Surface Science , 257, 2011. - p.5132–5137.

[8] Praveen A.S., et al.. Erosion wear behaviour of plasma sparyed NiCrSiB/Al_2O_3 composite coating, International Journal of Refractory Metals and Hard Materials 52, 2015. – p. 209–218.

[9] Umanskii, A.P., et al. Structure, phase composition, and wear mechanisms of plasma sprayed NiCrSiB-20 wt.% TiB_2 coating, //Powder Metallurgy and Metal Ceramics, 53 (11–12), 2015. - p. 663–671.

[10] Martin A., et al. Sliding wear behaviour of plasma sprayed WC-NiCrBSi coatings at different temperatures //Wear , 251, 2001. - p. 1017–1022.

[11] Niranatlumpong P., Koiprasert H. Phase transformation of NiCrBSi–WC and NiBSi–WC arc sprayed coatings, //Surface and Coatings Technology, 206, 2011. - p. 440–445.